Author Accepted Manuscript
This manuscript is the author accepted version of a paper published in
***Journal of Atmospheric and Solar–Terrestrial Physics* (2024).**
DOI: 10.1016/j.jastp.2024.106198

First results of the potential gradient variation in a tropical station in South America (Ica, Peru)

Rubén Romero[1,4], José Tacza[2,3,4], Joseph Arroyo[1], Francis Prieto[1], Edith Macotela[5], Yovanny Buleje[1], René Loayza[1], Ulices Fernandez[6], Jean-Pierre Raulin[4]
[1]Universidad Nacional San Luis Gonzaga, Ica, Peru.
[2]Institute of Geophysics, Polish Academy of Sciences, Warsaw, Poland.
[3]HUN-REN Institute of Earth Physics and Space Science, Sopron, Hungary.
[4]Center of Radio Astronomy and Astrophysics Mackenzie, Engineering School, Mackenzie Presbyterian University, São Paulo, Brazil.
[5]University of Bath, Bath, United Kingdom.
[6]Universidad Cientifica del Sur, Lima, Peru.

Abstract
Measurements of the potential gradient (PG) under fair weather conditions at new locations are crucial for monitoring the global electric circuit. In this study, we analyzed the variations in PG recorded in Ica city, Peru, during the period from March 2018 to December 2022. Our analysis involved a detailed comparison of PG with various meteorological parameters such as rainfall, wind speed and direction, dust storms, dust devils and fog to establish the characteristic PG curve under fair weather conditions (referred to as the standard curve). We identified a significant threshold of 3.5 m/s for strong winds, which helps prevent the influence of sea breeze and dust lifting on PG. Our results showed the impact of 'Paracas' dust storms on PG, which aligns with patterns observed in other arid regions worldwide. Subsequently, we calculated monthly, seasonal, and annual averages of the standard curve which showed a response likely associated with local convective processes on the PG diurnal variation. Furthermore, the seasonal variation of PG reveals higher values during June, July, and August compared to December, January, and February. These differences are attributed to seasonal changes in aerosol concentrations, potentially influenced by biomass-burning activities in Peru. Additionally, we performed a wavelet transform analysis of PG hourly values. We found the periodicities of 1 day, ~188 days, and 360 days which are related to the diurnal, semiannual and annual periods. During the months between January and March 2018 was found an intense period of ~45-day likely associated with one of the strongest Madden-Julian Oscillation events. Through this comprehensive investigation, we deepen our understanding of the intricate relationships among meteorological conditions, sea breeze, dust storms, and the PG in arid regions like Ica.

1. Introduction

Our planet can be conceptualized as a large spherical capacitor, with the Earth's surface acting as a good conductor of electricity, and the upper atmosphere serving as the second layer. The air between these two layers is a reasonably good electrical insulator (i.e., it is a leaky dielectric medium), forming what is known as the Global Electric Circuit (GEC) model. The GEC model describes the global-scale flow of electrical currents around the Earth, where mainly thunderstorms and electrified shower clouds charge the upper atmosphere, and the electrical currents return to the Earth's surface during fair weather conditions (Rycroft et al., 2008; Liu et al., 2010; Haldoupis et al., 2017).

From 1928 to 1929, the Carnegie Institution of Washington conducted numerous measurements of the atmospheric electric field across oceans worldwide. Later analysis revealed that the daily variation of

the electric field, measured in Universal Time (UT), was consistent regardless of the ship's location (Torreson et al., 1946). Moreover, under fair weather conditions, this daily variation exhibited an intensity of E = -130 V/m, with the negative sign indicating that the electric field vector points downward. This daily variation is commonly referred to as the 'universal' Carnegie curve (Harrison, 2013). Meteorologists use the term potential gradient (PG) to refer to the same concept as the atmospheric electric field (E). Both PG and E represent the same magnitude, but conventionally, the PG is considered positive in fair weather conditions. In this manuscript, we will adhere to the PG convention.

PG measurements worldwide are important to monitor the GEC. However, these measurements are often influenced by local effects such as pollution and meteorological parameters (Nicoll et al., 2019). Therefore, it is important to accurately identify PG perturbations related to local effects. Meteorological parameters, including rain precipitation, wind speed and direction, dust storms, and fog, are significant phenomena that affect PG locally.

Bennett and Harrison (2007) observed that cumuliform clouds, containing charged regions, can cause significant deviations in the surface PG, with deeper clouds often bearing higher charges and thus leading to larger PG deviations during their transit. Rainfall, often carrying a charge, contributes to these fluctuations; however, the deviations due to rain are typically short-term, with smaller magnitude variations compared to those induced by cloud passage. Telang (1930) supports this observation, indicating that the initial stages of rain can abruptly reverse the normally positive PG, with the effect dissipating rapidly after the rain ceases. Moreover, while light rain has been associated with a decrease in PG at the surface, the impact of convective precipitation with heavy rain and significant cloud base charge is more pronounced, resulting in greater variability in PG. Karagioras and Kourtidis (2021) further explored this by studying prolonged rainfall events, finding that extended precipitation can have a more sustained influence on PG, in contrast to the brief effects of lighter showers.

Changes in wind direction can significantly impact the PG by altering the concentration of aerosols and charged particles in the air, which subsequently affects the PG. For instance, if there are nearby sources of charge separation, such as dust sources and industrial smoke, a change in wind direction can transport these charged particles to the observation site, thereby influencing the PG. Consequently, short-term fluctuations in the PG can occur (Bennett and Harrison, 2007). Furthermore, strong winds can induce charge separation through interactions with the Earth's or water's surface, leading to changes in the PG at the surface. Nicoll et al. (2022) explored the impact of wind in desert regions, specifically due to the sea breeze in the United Arab Emirates. They concluded that sea breeze circulation, along with local convective processes, predominantly governs the daily variation of the PG, establishing new fair-weather criteria for arid zones to mitigate the influence of the sea breeze: wind speed between 1 and 5 m/s and visibility >25 km.

Similarly, the effects of dust and dust storms are well-documented phenomena. Electric fields generated during these storms exhibit a direct relationship with dust concentration, playing a crucial role in the phenomena of dominant volume charge observed during these events. It has been observed that the electric field can strengthen hours prior to the arrival of dust storms, providing a valuable tool for early and accurate detection of these events that surpass traditional terrestrial and spatial observations (Zhang et al., 2017; Williams et al., 2008). Additionally, the electric charge carried by dust and sand particles can increase the risk of fires and damage to electrical equipment, which has important implications for safety measures and infrastructure planning in areas affected by these dust storms. Dust devils (small, brief whirlwinds occurring most frequently in the early afternoon when a land surface is heating rapidly) are more common in desert and arid terrains, characterized by large expanses of dry, vegetation-free soil that cannot retain moisture (Bagnold, 2012). Franzese et al. (2018) found a linear relationship between the electric field and the concentration of particles lifted in dust devils, which aligns with the findings of Esposito et al. (2016), indicating that the charging process depends not only on the grain size but also on the composition of the dust particles. Duff and Lacks (2008) conducted a study demonstrating that

triboelectric charging can occur in granular systems consisting of particles of the same composition. They observed that smaller particles tend to charge negatively, while larger ones charge positively. Furthermore, they found that the magnitude of triboelectric charging increases when there is a wide variety in the particle size distribution.

Fog and mist phenomena, characterized by the presence of suspended water droplets in the air, lead to a reduction in visibility. According to the Glossary of Meteorology (American Meteorological Society, 2023), the primary distinction between the two lies in the extent of reduced visibility. Fog is defined as visibility reduced to less than 1 kilometer, while mist reduces visibility to a range of 1 to 5 kilometers. Current research has shown that fog tends to amplify the PG due to larger droplets impeding the mobility of charge carriers. Consequently, in accordance with Ohm's law, this reduction in conductivity leads to an increase in the PG (Anisimov et al., 2005; Bennett and Harrison, 2009; Yair and Yaniv, 2023). Additionally, it is noteworthy that the PG can respond to fog nuclei before the fog itself becomes visible. This observation holds practical implications for short-term fog prediction (Bennett and Harrison, 2007).

As mentioned earlier, meteorological parameters have an impact on the PG. Therefore, it is essential to analyze the PG before studying any global influences. Currently, there are numerous PG stations around the world dedicated to studying the Global Electric Circuit (GEC). For instance, the GloCAEM (Global Coordination of Atmospheric Electricity Measurements) network consists of 23 PG stations. Through the analysis of PG data from these locations, researchers can obtain more detailed information on the daily variability of the GEC, leading to a better understanding of the factors influencing the GEC, including climate variations and space weather effects (Nicoll et al., 2019). Nevertheless, the installation and meticulous analysis of additional PG stations are still required to advance GEC research.

In this study, we present five years of PG data recorded at Ica, Peru (Geographical coordinates: latitude: 14.089°S, longitude: 75.736°W, altitude: 406 masl) spanning from March 2018 to December 2022. As a first step, we conducted a comprehensive analysis of various meteorological parameters and their relationship with the PG. Subsequently, fair weather conditions at Ica station were defined. Secondly, we obtained the typical diurnal curve of the PG under fair weather conditions (referred to as the standard curve). Thirdly, a spectral technique (the wavelet transform) was employed to determine the dominant periodicities. In Section 2, we provided information about the PG site measurement, instrumentation, and data analysis employed in this study. The results are presented and discussed in Section 3.1 and 3.2 (temporal analysis) and Section 3.3 (spectral analysis). Finally, the main findings are summarized in the last section.

2. Description site, Instrumentation and Data Analysis

2.1 Description Site

Ica is located on the south-central coast of Peru at an altitude of 406 meters above sea level (m.a.s.l.). It is a rugged desert region surrounded by mountain ranges, valleys, hills, and dunes, with oases and extensive pampas in its vicinity. The city is situated on an alluvial plain formed by the Ica riverbed and exhibits a significant amount of eolian deposits, comprising dry and loose sand that migrates due to wind activity, giving rise to dunes and sandbanks. The climate is characterized as warm and arid, with an average annual temperature of 21°C and minimal annual precipitation (Haney and Grolier, 1991; Gay, 2005; Davila et al., 2021). Ica city experiences an arid subtropical climate, which results in occasional and low-intensity rainfall occurring primarily between January and March. The intensity of rainfall in Ica can be influenced by climatic phenomena, including the El Niño phenomenon, which can lead to heavy rainfall along the coast of Peru (Davila et al., 2021).

Situated 60 km from the coast, Ica city is occasionally affected by dust storms known as ‘Paracas’ winds. These winds originate from the Paracas-Pisco coast, primarily between July and September, specifically

between 12:00 and 17:00 hours (local time), with surface velocities reaching approximately 17 m/s. The mechanisms responsible for triggering the Paracas winds remain unidentified; however, recent research indicates that local topography and the shortwave radiation reaching the ground contribute to the intensification of wind and turbulence required for the occurrence of this phenomenon (Quijano, 2013).

Figure 1 presents an informative color map illustrating the topography of Ica, emphasizing the variations in altitude. The map uses gray shades to represent higher altitude areas, while colorful tones indicate lower altitude regions. It is evident that the city is situated in a valley surrounded by elevated terrain, resulting in a distinctive wind pattern. According to Gay (2005), sand-bearing winds converge from different directions, specifically from the northwest, west, southwest, and southeast. The author concludes that the sand originates from the Pacific Ocean beaches, transported inland by predominantly south-southeast winds, and eventually settles in substantial sand masses, typically found at higher elevations.

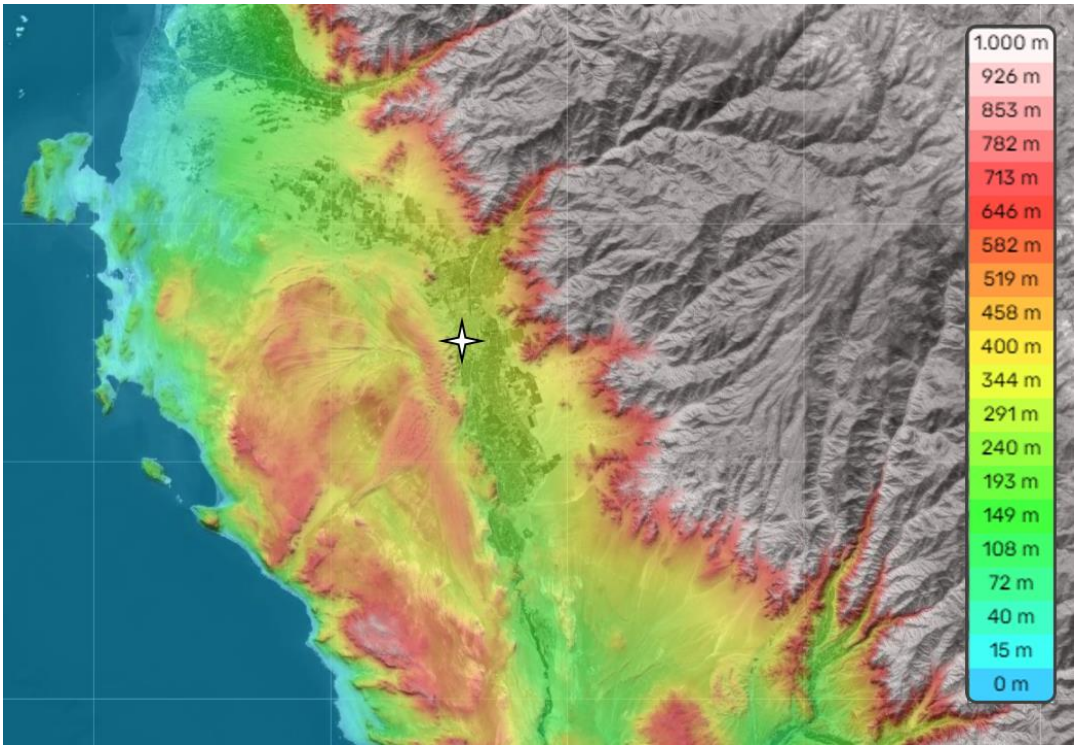

Figure 1. Topography of Ica city. The star denotes the sensor's location. Data retrieved from www.topographic-map.com

2.2 Instrumentation

Ica station is part of a network of 9 electric field mill stations situated in various locations across South America (Tacza et al., 2020). The BOLTEK EFM-100 sensor is employed for PG measurements, which operates based on electrostatic induction: when a conducting plate is exposed to an electric field, a charge is induced proportionally to the electric field strength and plate area (Imyanitov, 1957; Secker, 1975; MacGorman and Rust, 1998). The EFM has a dynamic range of ±20 kV/m, and the measurements are recorded at a temporal resolution of 0.05 s. Although the sensor was initially installed in December 2011, it recorded quase-constant measurements until December 2014. After that, sporadic measurements were taken until 2017. Tacza et al. (2020) described the PG measurements recorded from 2011 to 2014. Since February 2018, the sensor has been continuously recording PG measurements. It is located at the facilities of the Center for Research on Solar Activity and its Effects on Earth (CIEASEST), within the San Luis Gonzaga National University of Ica (14.089°S, 75.736°W, altitude: 406 masl). In addition to the EFM sensor, at CIEASEST there is installed a meteorological station, situated 50 meters away from the field mill sensor. It is an automatic Campbell station equipped with a pyranometer, anemometer,

thermometer, hygrometer, and barometer. It collects data with a temporal resolution of 10 seconds and was installed in July 2019.

2.3 Data analysis

The field mill sensor is positioned at a height of 0.5 m above the ground, resulting in an overestimation of the PG values. To account for this, the PG values were corrected using a reduction factor (Tacza et al., 2020). Figure 2a presents the time series of PG hourly measurements at the ICA station, while Figure 2b illustrates the distribution of PG hourly values. The PG mean and PG median values are 68 V/m and 50 V/m, respectively.

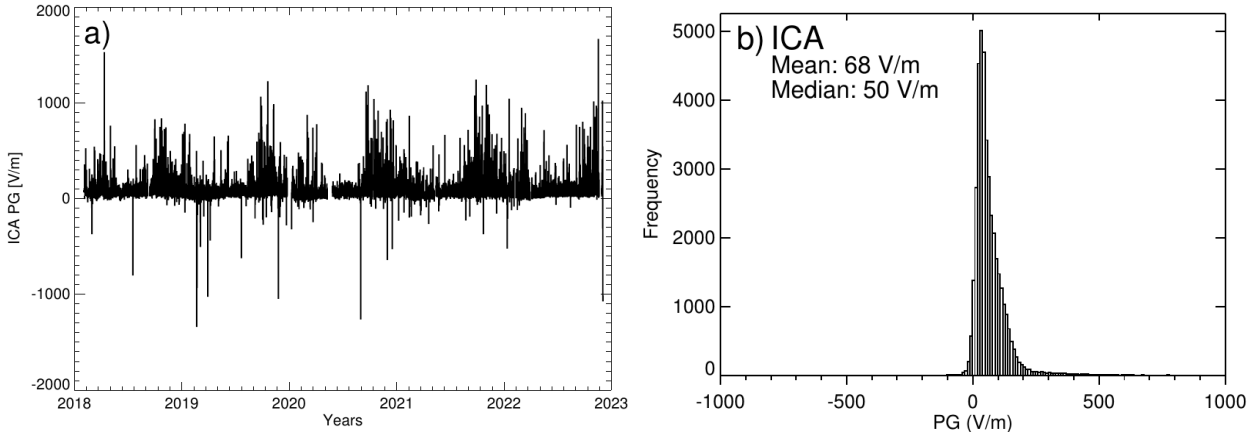

Figure 2. (a) Time series and (b) histogram of PG hourly mean values at Ica station.

In order to try to obtain a PG daily variation that represents a global pattern, it is necessary to consider 'fair weather' conditions. The UK Meteorological Office has defined fair weather since 1964 as weather conditions that satisfy specific criteria, including 3/8 of the sky being clear of cloud formations, absence of rain precipitation, and no extreme wind conditions (Harrison, 2013). Figure 3a presents a comparison of PG values during fair weather days, while Figure 3b illustrates the corresponding values during disturbed weather days. However, previous studies have emphasized the importance of defining fair weather conditions based on site-specific measurements (Tacza et al., 2020, 2021; Nicoll et al., 2022). In section 3.1, we conducted a comprehensive analysis of the PG variation under various meteorological conditions, identifying the optimal conditions specific to the Ica station. Subsequently, we computed the PG monthly, seasonal and annual variation specifically for fair weather conditions in section 3.2.

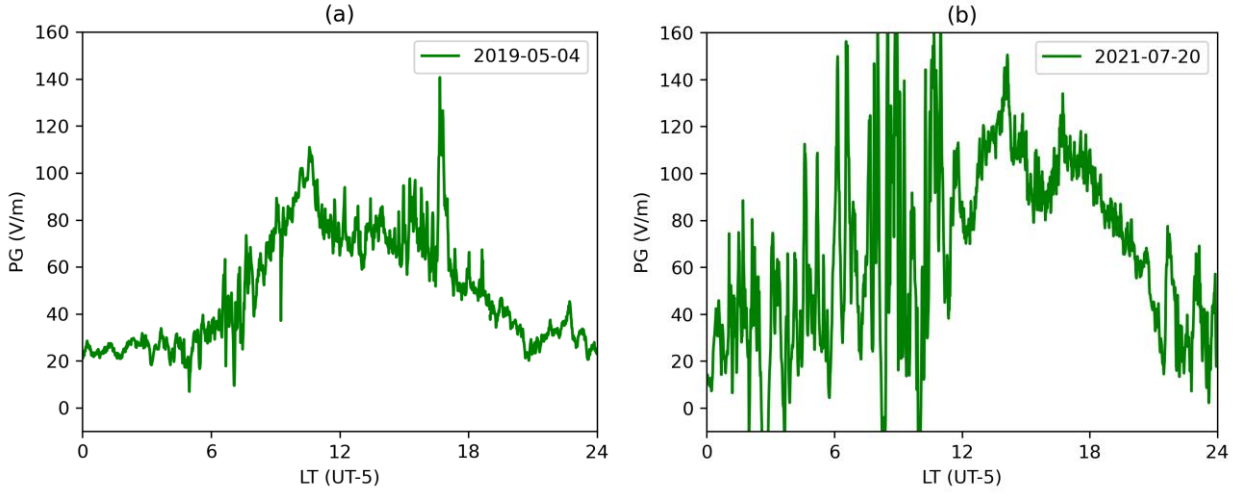

Figure 3. (a) PG during fair weather conditions. (b) PG during disturbed weather conditions.

In section 3.3, we used the wavelet transform to investigate the presence of regular short-term oscillations in the PG values. The wavelet analysis is a technique employed to extract both dominant

modes and their temporal variations from a time series (Torrence and Compo, 1998). In this study, the continuous wavelet transform toolbox for MATLAB package (Grinsted et al., 2004) is employed, taking in account the bias correction as indicate by Liu et al (2007).

3. **Results and discussion**

3.1 PG analysis versus meteorological parameters

As mentioned earlier, the local meteorological parameters, including rain precipitation, fog, strong wind speed, have a significant impact on the PG. At Ica station, the PG is expected to be strongly influenced by aerosol concentration, which is in turn influenced by the speed and direction of the wind. The wind plays a crucial role in lifting dust particles from the surface, which can lead to the formation of dust storms or dust devils. Despite a few rain precipitation and fog events at Ica, these parameters are also worth studying. All these events can affect the electrical conductivity, therefore influencing the PG at the site measurement. For all these reasons, in this paper we studied the effect of rain precipitation, wind speed and direction, dust devils and fog on the PG values recorded at Ica station.

3.1.1. Rain precipitation

Figure 4 illustrates the PG variation during a rainy day (green curve) compared to the monthly mean variation of the PG under fair weather conditions (standard curve, hereafter referred to as Std Curve, red curve) as reported by Harrison (2013). This pattern is consistent with findings from other researchers (Telang, 1930; Bennett and Harrison, 2007; Karagioras and Kourtidis, 2021). Due to the significant fluctuations in the PG caused by rainfall, we excluded rainfall days from the subsequent analysis.

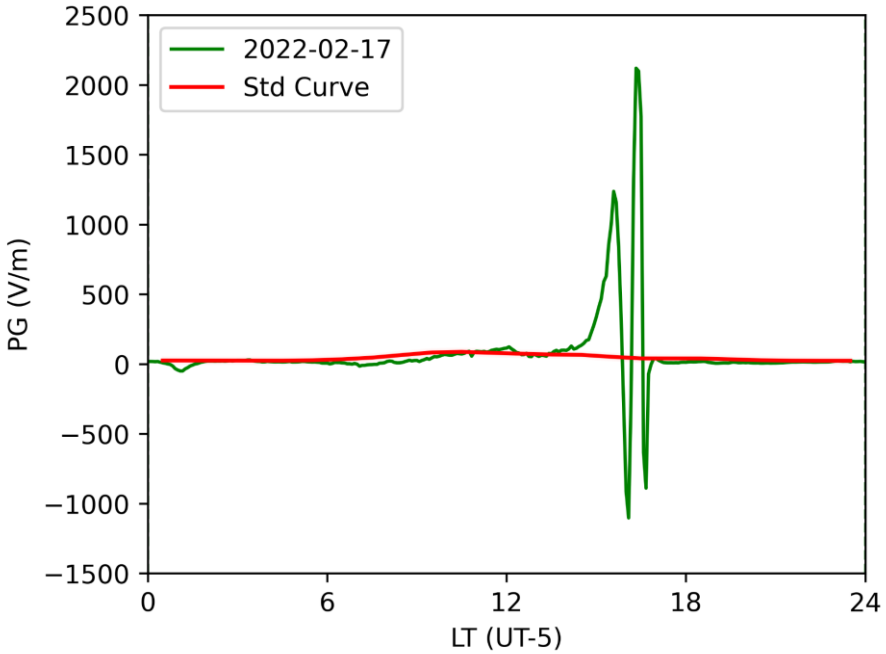

Figure 4. Typical variation of PG during rain precipitation in Ica. The green curve represents the PG daily variation on February 17, 2022. The red curve depicts the mean monthly average using fair weather conditions reported by Harrison (2013). The time resolution is 5 minutes.

3.1.2. Wind speed

As explained in section 2.1, Ica station is located in a region characterized by a desert climate with strong winds. The winds in Ica are strongly influenced by the local topography and the sea breeze (Haney and Grolier, 1991; Gay, 2005; Davila, 2021). Figures 5a to 5f present hexbin plots illustrating the relationship between PG and wind speed, chosen for their effectiveness in representing the density of data points, which is indicated on a logarithmic scale for clarity.

Figure 5 illustrates the fluctuation of PG in response to strong winds, analyzed (a) annually and on a (c-f) seasonal basis, which may be attributed to the transport of aerosols from various sources. In spring (Figure 5f), the greater dispersion of the PG is likely due to stronger winds, driven by the proximity of the South Pacific Anticyclone (SPA) to the coast, whose influence is more pronounced in winter and spring (Correa et al, 2020; Dewitte et al, 2011). Although the SPA intensifies coastal winds in winter, the specific terrain configuration and the microclimate of Ica (located 60km from the coast and in a valley) might attenuate its influence in this region, resulting in lesser PG dispersion. With the onset of spring and the consequent rise in temperatures, a notable change in wind patterns occurs, which reinforces the dispersion of PG. This tendency diminishes in summer and fall, in line with the decreased influence of the SPA.

Notably, Figure 5b, which depicts the relationship between the absolute value of the PG and the wind speed, with a 60-minute average, exhibits a distinct exponential increase in PG beyond a wind speed threshold of 3.5 m/s reflecting a consistent pattern across both positive and negative polarities of PG. Gay (2005) explored the intricate wind patterns in the region, which enable the northwest winds to carry sand and dust from the beaches, while southward winds transport distinct particles. These wind activities play a significant role in the accumulation of sand in the Ica sand bank, which receives sand from multiple directions, covering an angular span of 140 degrees. Similarly, Briceño-Zuluaga et al. (2017) conducted an analysis of Paracas dust storms in the Pisco-Ica region and identified multiple sources of sand and dust located to the north, west, and south of Ica, utilizing MODIS images and HYSPLIT model trajectories. The combined impact of these wind patterns can potentially affect particulate levels, leading to changes in PG.

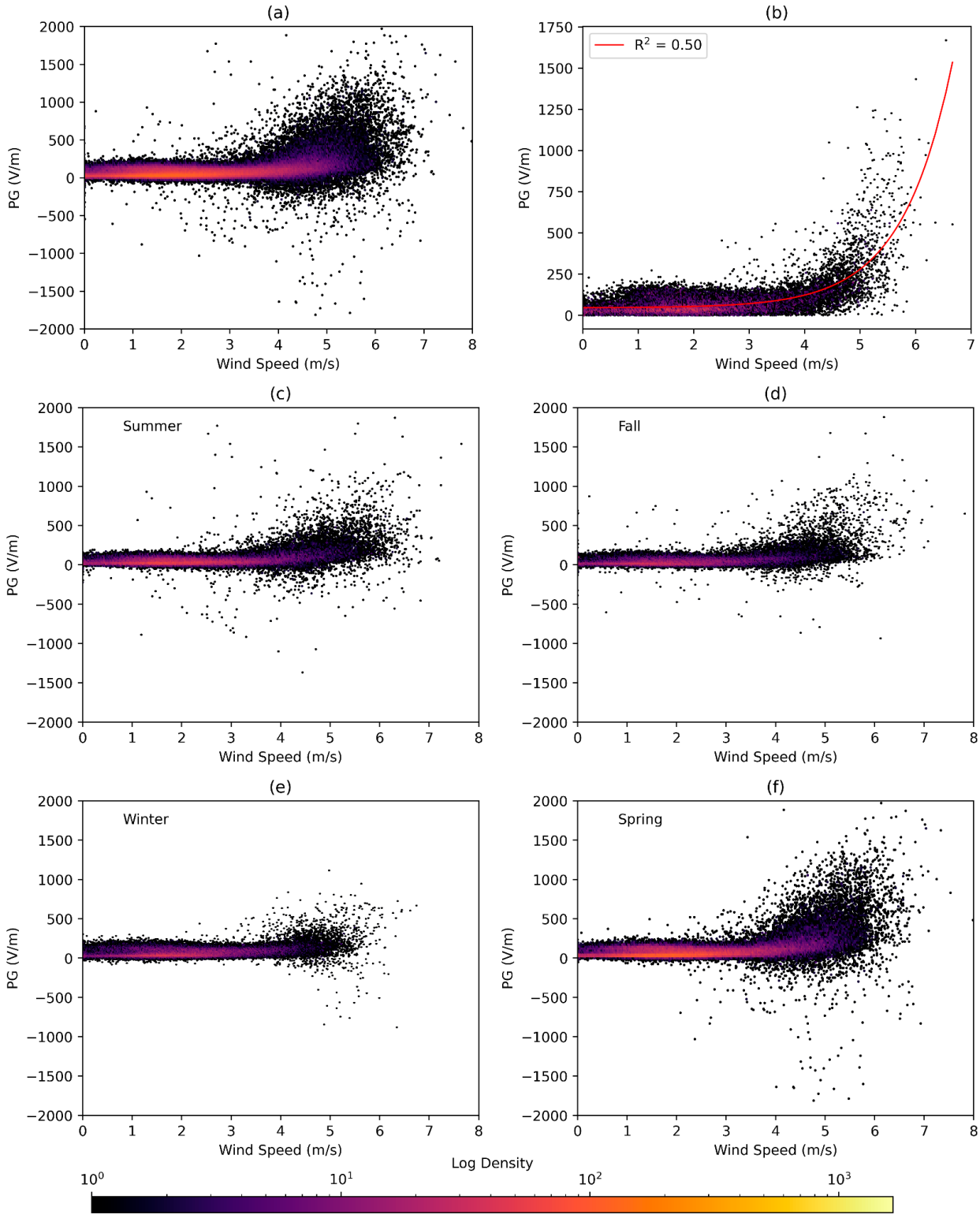

Figure 5. Hexbin plot showing the relationship between PG and wind speed, for the entire period with a 5-minute mean (a). Hexbin plot showing the relationship between the absolute value of PG and wind speed, averaged over 60 minutes, demonstrating an exponential trend line with an R-squared value of 0.50 (b). Seasonal variations are shown in (c-f) with a 5-minute average. Days where rain precipitation occurred were excluded from the analysis in all scenarios.

Based on the findings in Figure 5, we determined a threshold wind speed of 3.5 m/s, beyond which the PG exhibits disturbance. Subsequently, a dispersion graph was constructed to assess the potential commonality of the dust or sand carried by the wind. Figure 6 illustrates the variation of PG in relation

to wind direction across different seasons, where the same seasonal behavior (stronger winds in spring) is observed, associated with the proximity of the SPA. Wind speeds below 3 m/s were excluded to eliminate fair weather values. Notably, distinctive wind directions such as south-southeast (SSE) and northwest (NW) are observed, resulting in diverse polarities in the PG. Importantly, days characterized by strong northwest (NW) winds typically exhibited clear skies, which was corroborated both by irradiance data from the meteorological station and through empirical observations (by eye observation). On the other hand, days influenced by strong south-southeast (SSE) winds often experienced reduced visibility due to the occurrence of Paracas dust storms. Drawing from these findings and incorporating the insights of Gay (2005) and Briceño-Zuluaga et al. (2017), we can establish a correlation between the strong NW winds and the sea breeze, and the strong SSE winds and the Paracas dust storms.

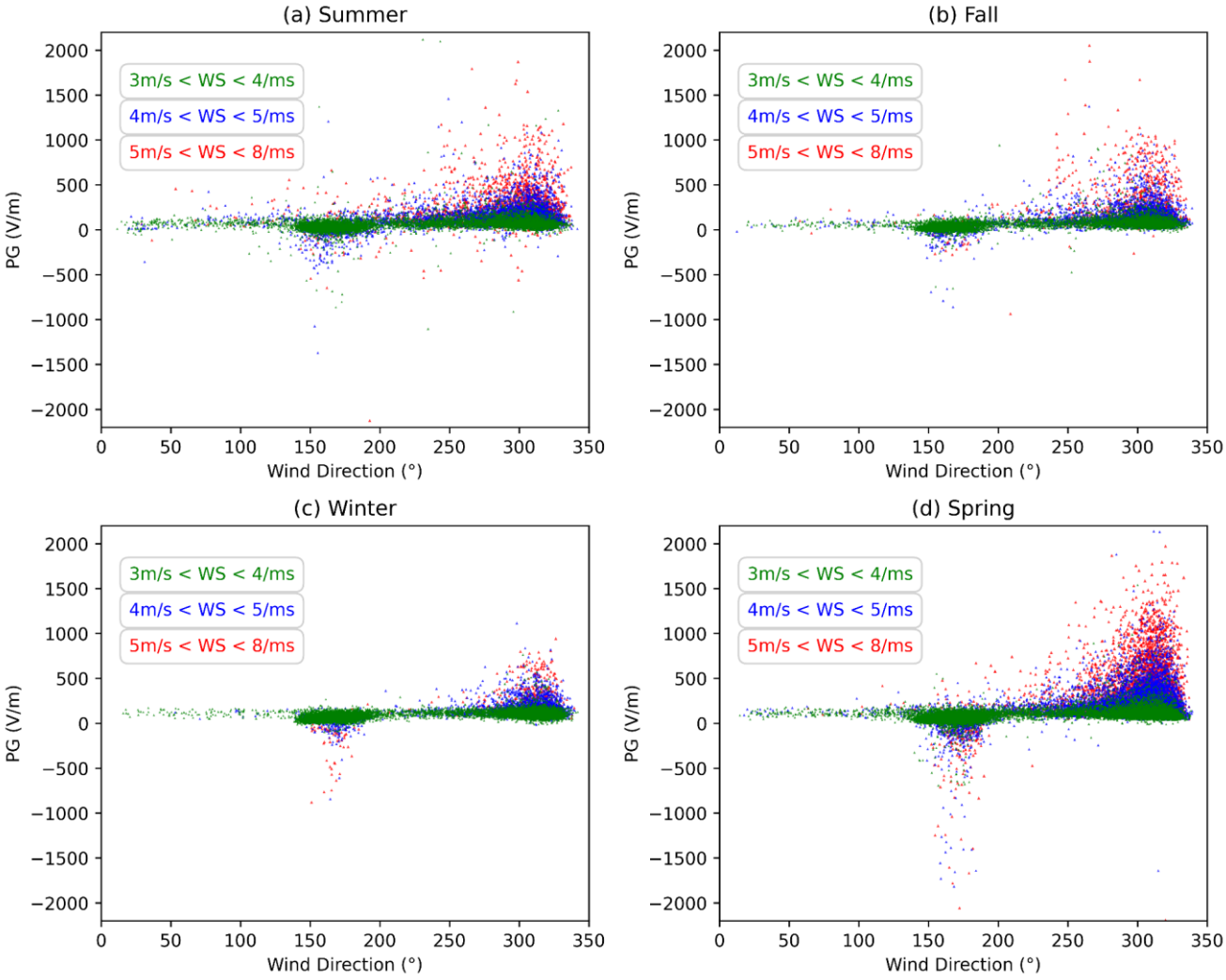

Figure 6. Seasonal scatter plots illustrating the relationship between PG and wind direction, with a 5-minute average. Green points represent wind speeds between 3 and 4 m/s, blue points represent wind speeds between 4 and 5 m/s, and red points represent wind speeds between 5 and 8 m/s. Rainy days and data points with wind speeds less than 3 m/s were excluded.

Figures 7 and 8 depict two notable events characterized by strong NW and SSE winds, respectively, exhibiting distinct effects on PG. Figure 7a shows the PG values during November 18th, 2022. This day was selected due to the significant PG increase, likely associated with a robust sea breeze. Figure 7b shows that the wind speed values peaked at 7 m/s, aligning with the PG increase. Furthermore, Figure 7c displays the wind direction values, revealing a consistent pattern between 13 and 20 LT, indicative of the duration of the marine breeze. A separate sea breeze case study took place on November 7th, 2022. Figures 7d, 7e, and 7f present the variation in PG, wind speed, and wind direction, respectively,

throughout that day. The wind speed reached a maximum of 6 m/s, coinciding with the PG increase. Figure 7f displays the wind direction values, providing insight into the duration of the sea breeze.

Figure 8a shows the PG values during September 1, 2022. This day was selected due to the significant PG decrease, likely associated with a Paracas wind. In Figure 8b, it is evident that the wind speed remained consistently high throughout the day, peaking at 7 m/s, while Figure 8c depicts constant wind direction originating from the SSE throughout the day. Additionally, another case study involving the Paracas winds occurred on January 12th, 2022, as depicted in Figures 8d, 8e, and 8f. Notably, Figure 8e displays a lower wind speed, peaking at 5 m/s. Figure 8f presents the wind direction values, indicating the predominance of SSE winds throughout the event.

In Figure 9, we employed the HYSPLIT tool to verify the origin of air masses reaching the Ica station, attributed to aerosol particles carried by the sea breeze on November 18th, 2022, and the Paracas winds on September 1st, 2020. The selected hours corresponded to when the PG attained its maximum amplitude. Back-trajectory lines are depicted in red/purple, blue/orange, and green/yellow, representing altitudes of 100, 300, and 500 meters above ground level, respectively. This analysis validates the suspended dust and sand's source for each event, aligning with the observations made at the meteorological station.

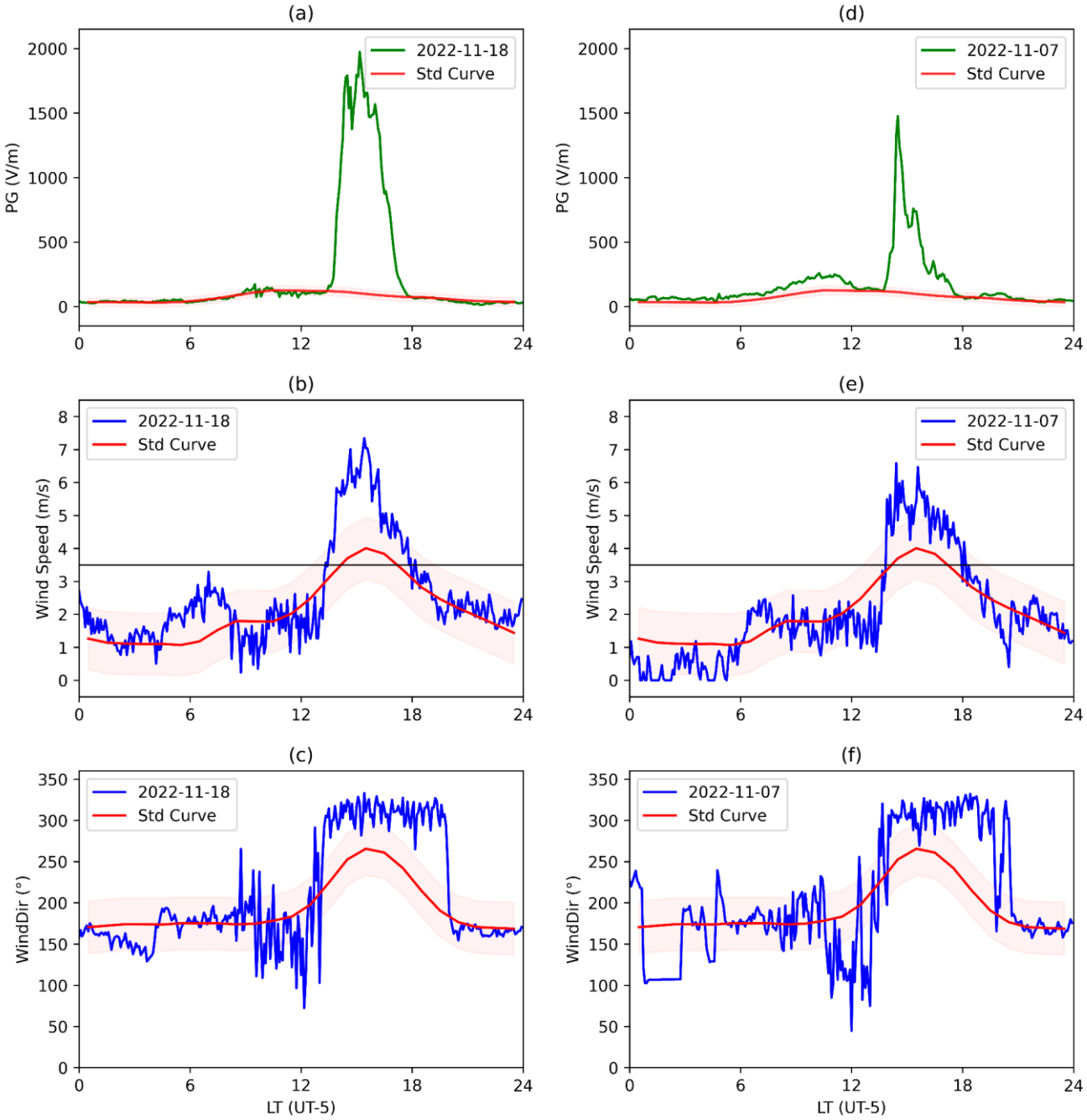

Figure 7. (a) PG daily variation, (b) wind speed, and (c) wind direction on November 18, 2022. (d), (e), and (f) represent the same variations but for November 7, 2022. In both study cases, a strong sea breeze was reported. The red curve represents the monthly mean daily variation for each parameter under fair weather conditions, with error bars indicating one standard deviation.

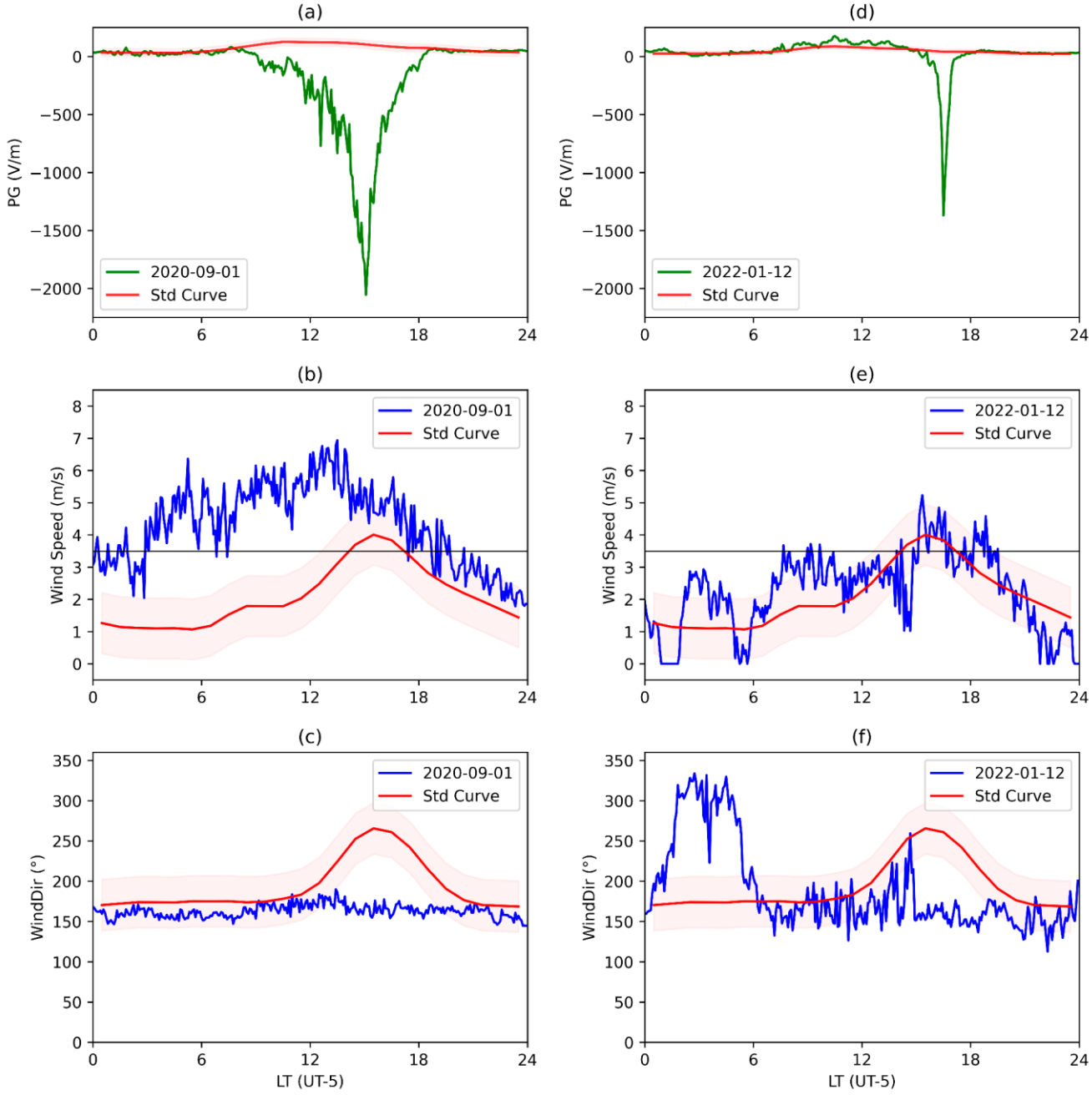

Figure 8. (a) PG daily variation, (b) wind speed, and (c) wind direction on September 1, 2020. (d), (e), and (f) represent the same variations but for January 12, 2022. In both cases, a Paracas dust storm was reported. The red curve represents the monthly mean daily variation for each parameter under fair weather conditions, with error bars indicating one standard deviation.

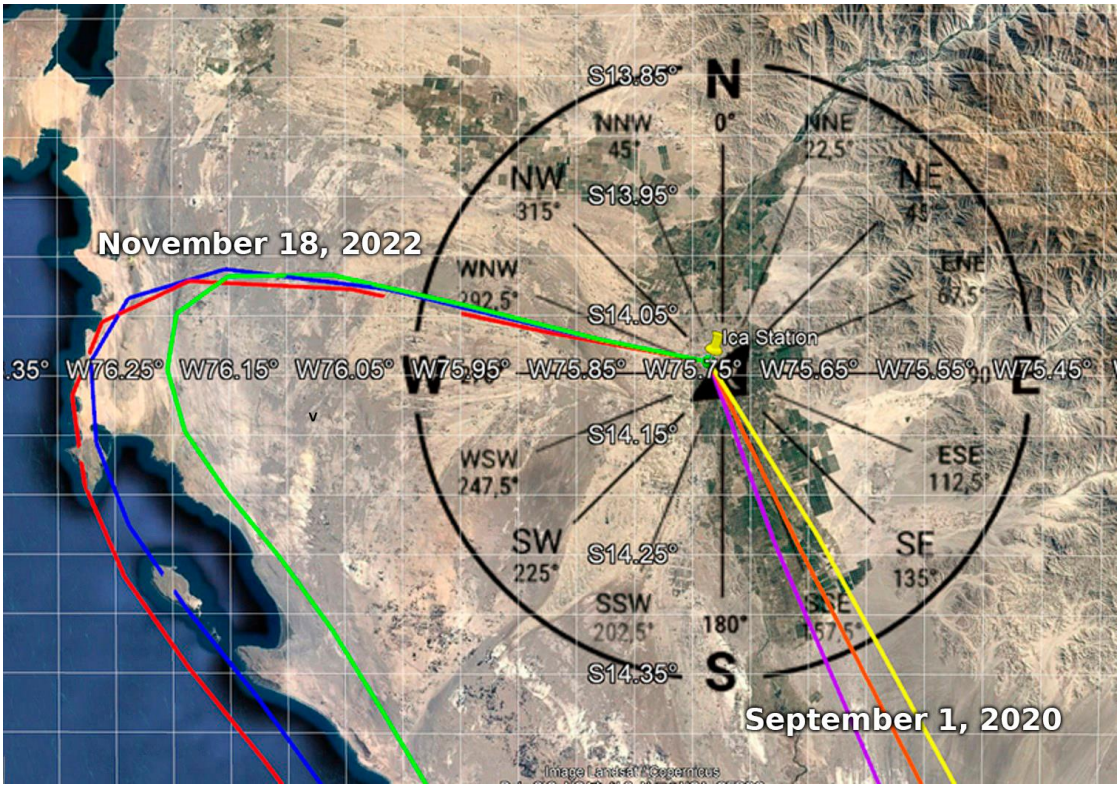

Figure 9. Back-trajectory analysis of the air masses reaching the Ica station on November 18, 2022, depicted in red, blue, and light green colors, and on September 1, 2020, depicted in purple, orange, and yellow colors. The map was generated using the HYSPLIT tool. Red/purple represents air masses at 100 meters above ground level, blue/orange represents air masses at 300 meters, and light green/yellow represents air masses at 500 meters.

The sea breeze was responsible for PG increases on approximately 44% of days per year, while strong SSE winds and low dust density in the environment led to PG decreases on 12% of days per year. Interestingly, 84% of these days with decreased PG did not exhibit a concurrent reduction in visibility, as determined through visual assessment using a camera focused on the sensor. It is important to note that this observation does not rule out the presence of dust in the environment. Additionally, 10 occurrences of Paracas dust storms were recorded, which were marked by a substantial decrease in visibility. The reduction in PG preceding a dust storm due to the presence of suspended dust in the air has been extensively documented in the literature (Rudge, 1913; Kamra, 1972; Zhang et al., 2017). Furthermore, the seasonal occurrence of the sea breeze peaks in Summer and Spring, with the same frequency of 59% of days, and a minimum in Winter (18%), while dust events have a maximum occurrence in Spring (18% of days) and a minimum in Winter (6%). This behavior is supported by the PG dispersion shown in Figure 5.

Figures 10a, 10b, and 10c present histograms showing the distribution of PG, wind direction, and wind speed, respectively, during the hours when Paracas dust storms occurred. In a similar way, Figures 10d, 10e, and 10f show the same parameter variation when strong sea breezes occurred. For both, dust storms and sea breeze, we chose the 13 strongest events. Sea breeze days exhibit PG amplitudes of up to 2000 V/m, while Paracas dust storm days show amplitudes of up to -2000 V/m. Additionally, a clear concentration of south winds (160°) is observed during Paracas dust storms, whereas northwest winds (310°) prevail during sea breeze events. Importantly, it should be noted that the threshold values for wind speed differ between the two phenomena, with sea breeze days requiring a threshold of approximately 4 m/s, while Paracas dust storms exhibit a lower threshold, possibly due to differences in wind current origins.

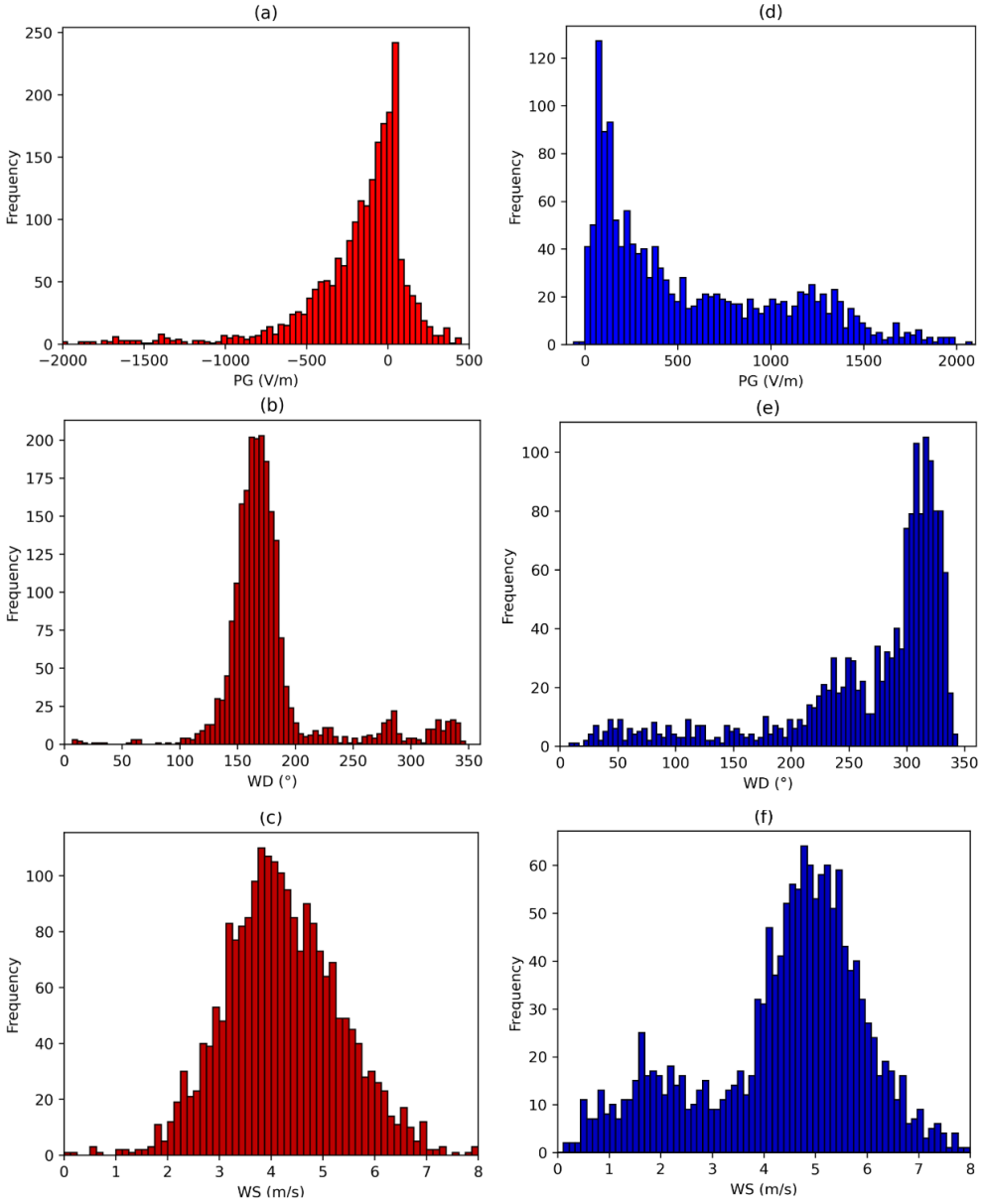

Figure 10. Red: Histograms showing the distribution of (a) PG, (b) wind direction, and (c) wind speed for 13 days displaying PG decreases associated with Paracas dust storms. Blue: Histograms illustrating the distribution of (d) PG, (e) wind direction, and (f) wind speed for 13 days exhibiting increases in PG associated with the strong sea breeze.

3.1.3 Dust Devils

At Ica station, PG deviations were observed during the passage of several dust devils in close proximity to the sensor. In this study, we focused on three prominent events, as illustrated in Figures 11 and 12. The observed 4-second PG increases in Figure 11a can be attributed to the influence of a positively charged region within the dust devil, resulting in an elevated PG. These findings align with the observations made by Lorenz et al. (2016), who documented a consistent electrical current signature in various dust devil events. The current initially increased leading up to the closest approach and subsequently transitioned to a decaying negative current as the dust devil moved away. A photograph capturing the dust devil in closest proximity to the EFM sensor is presented on the right side of Figure 11a, coinciding with the moment of maximum PG variation. It is important to note that in this event the dust devil never passed over the sensor, which would explain the only increase in PG due to the influence of the positive space charge on the sensor.

On the other hand, Figure 11b illustrates a typical PG measurement when a dust devil passes over the sensor. The observed 20-second decrease in PG can be attributed to the sensor being shielded by a dust cloud, which carries a negative charge due to the triboelectric effect, resulting in an upwardly oriented field. This phenomenon is widely reported in the literature (Freier, 1960; Farrell et al., 2004; Crozier, 1964, 1970; Bo and Zheng, 2013). Figure 12 shows the largest and longest-lasting dust devil recorded during the study period. It exhibits two distinct patterns of PG variations: a gradual decrease when the dust devil is situated tens of meters away, yet at a sufficient height to disperse dust near the EFM sensor, followed by an increase as it approaches within a few meters, culminating in a maximum decrease upon reaching the sensor. This initial behavior of the gradual drop of PG to the first minimum of -3000V/m could be due to the fact that at that distance the dust devil would act as a small dust storm which has been shown to have a consistent negative impact on the sensor. However, the recovery up to -2000V/m when the dust devil is much closer to the sensor would be consistent with the positive current transfer mentioned by Lorenz et al. (2016) until it reaches the sensor causing the maximum drop in PG due to the influence of its negatively charged base which is observed in Figure 12d.

While our study provides valuable insights, it's also useful to consider some areas for enhancement in future research. The meteorological station, located 50 meters from the PG sensor, was not in the direct path of the dust devils, which limited our ability to capture certain direct measurements of these phenomena. Additionally, our current setup did not include specialized equipment like electric current sensors or dust traps. Such tools would be instrumental for a more in-depth analysis of the composition and electrical properties of dust devils. Future studies, equipped with a broader range of sensors, including those for direct current measurement and dust analysis, could enrich our understanding of the electrical characteristics of dust devils. This advancement would offer more comprehensive insights into their composition, charge distribution, and overall dynamics, as well as their interactions with the PG.

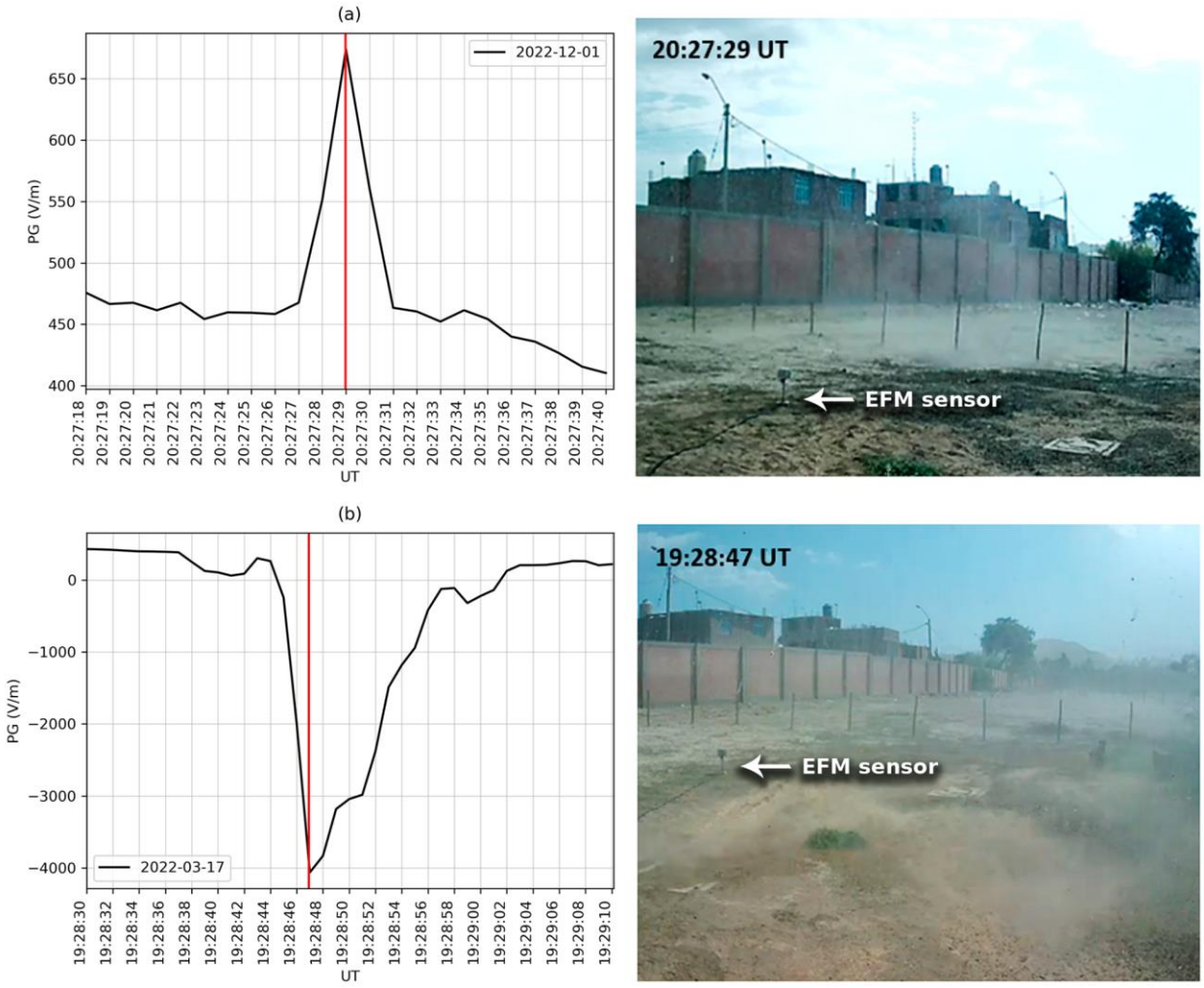

Figure 11. (a) PG increases resulting from a dust devil passing near the EFM sensor. (b) PG decreases caused by a dust devil passing over the EFM sensor. Red vertical lines indicate the maximum PG variation and the corresponding time of the photo on the right. It is noteworthy that the duration of the high PG variation is extremely short, on the order of a few seconds.

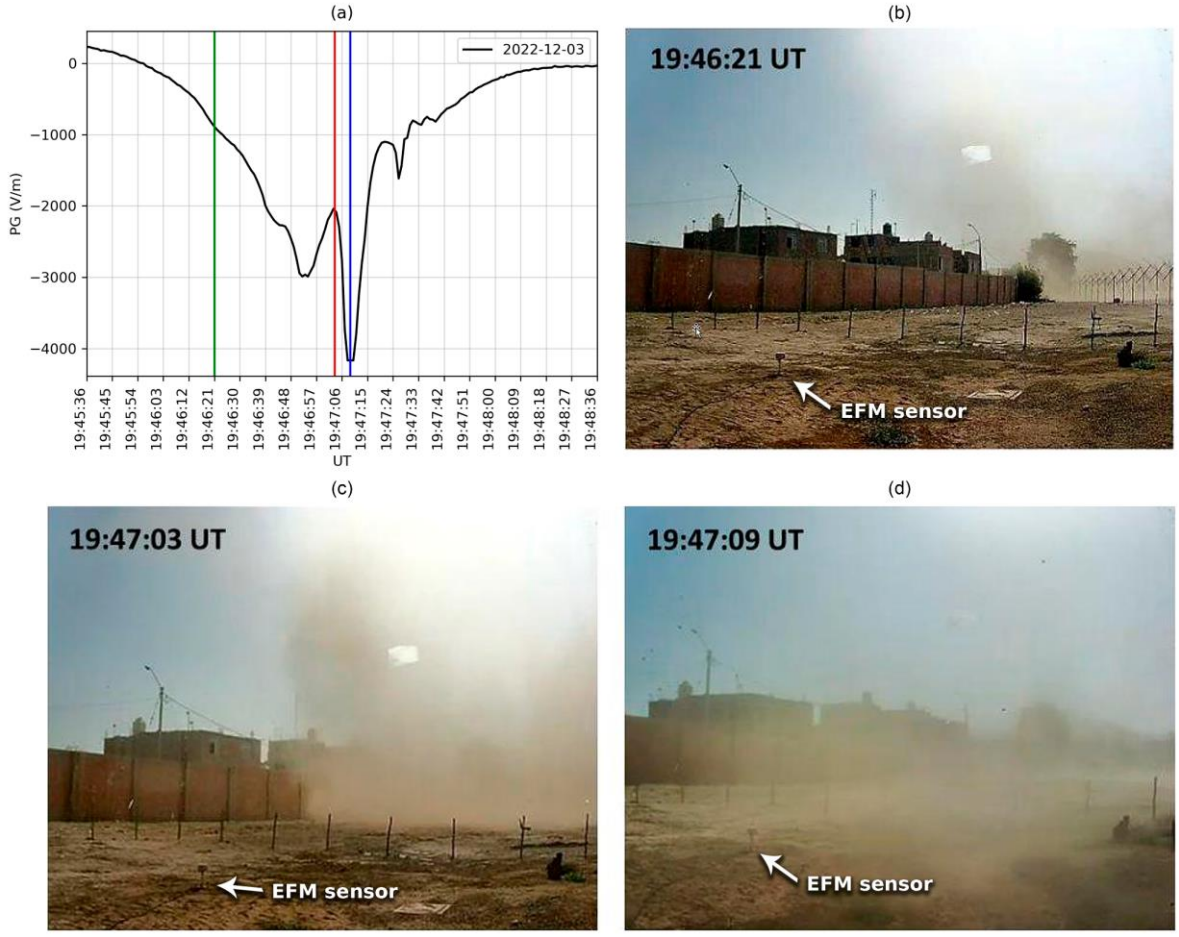

Figure 12. (a) PG variation showing the observed fluctuations as a dust devil passes near and over the sensor, with a photo taken at the exact moment of maximum increase and decrease. (b), (c), and (d) are photos taken at the times corresponding to the green, red, and blue vertical lines, respectively.

3.1.4 Fog

It is widely acknowledged by multiple authors that PG tends to increase during fog due to the reduced electrical conductivity caused by the presence of water droplets in the air (Anisimov et al., 2005; Bennet and Harrison, 2009; Yair and Yaniv, 2023). For this reason, we investigated the influence of fog on the PG values recorded at ICA. Figures 13a, 13b, and 13c show the daily variation of relative humidity, wind speed, and PG during a dense fog event that occurred on June 28, 2021. This study case was identified through a photograph at the site measurement at 07:43 LT (Figure 13d). The observations indicated that PG values tend to increase when the relative humidity reaches 100% and the wind speed is below 2 m/s.

On the other hand, Figure 14 shows another study case that occurred on July 20, 2021 when the fog was less dense (Figure 14d). There is not a significant PG increase even at RH = 100%, however some PG oscillations are observed. Note that wind speed are between 2 and 3 m/s. The PG oscillations are likely attributed to the irregular movement of the fog as it interacts with the sensor, transitioning between clear and foggy conditions. Similar results were found by Yair and Yaniv (2023).

Clouds and fog are both visible manifestations of atmospheric water, differing only in their altitude. Fog can be regarded as a stratus cloud positioned close to the ground (Lakra and Avishek, 2022). In Ica, 95% of the days with fog exhibit PG variations similar to those observed by Harrison et al. (2008, 2017) during nearly 40% of winter days. These studies demonstrate that swift changes in the height of cloud bases impact PG, attributable to the dominant negative charge present in the lower cloud layers. Conversely, only 5% of the foggy days exhibit a consistent increase in PG without oscillations. Fog is prevalent in Ica during the winter season (June to August). Additionally, we used the proximity of the sensor to a dune, employing the criteria established by the Glossary of Meteorology (AMS 2023), to distinguish between fog and mist based on the visibility of the dune. Although both events depicted could be classified as fog, they exert varying effects on PG. During the 4-year study period, we observed over a hundred days characterized by PG oscillations (as shown in Figure 3b and 14c) that were associated with fog and mist. Conversely, the occurrences of elevated PG levels specifically linked to fog were relatively rare.

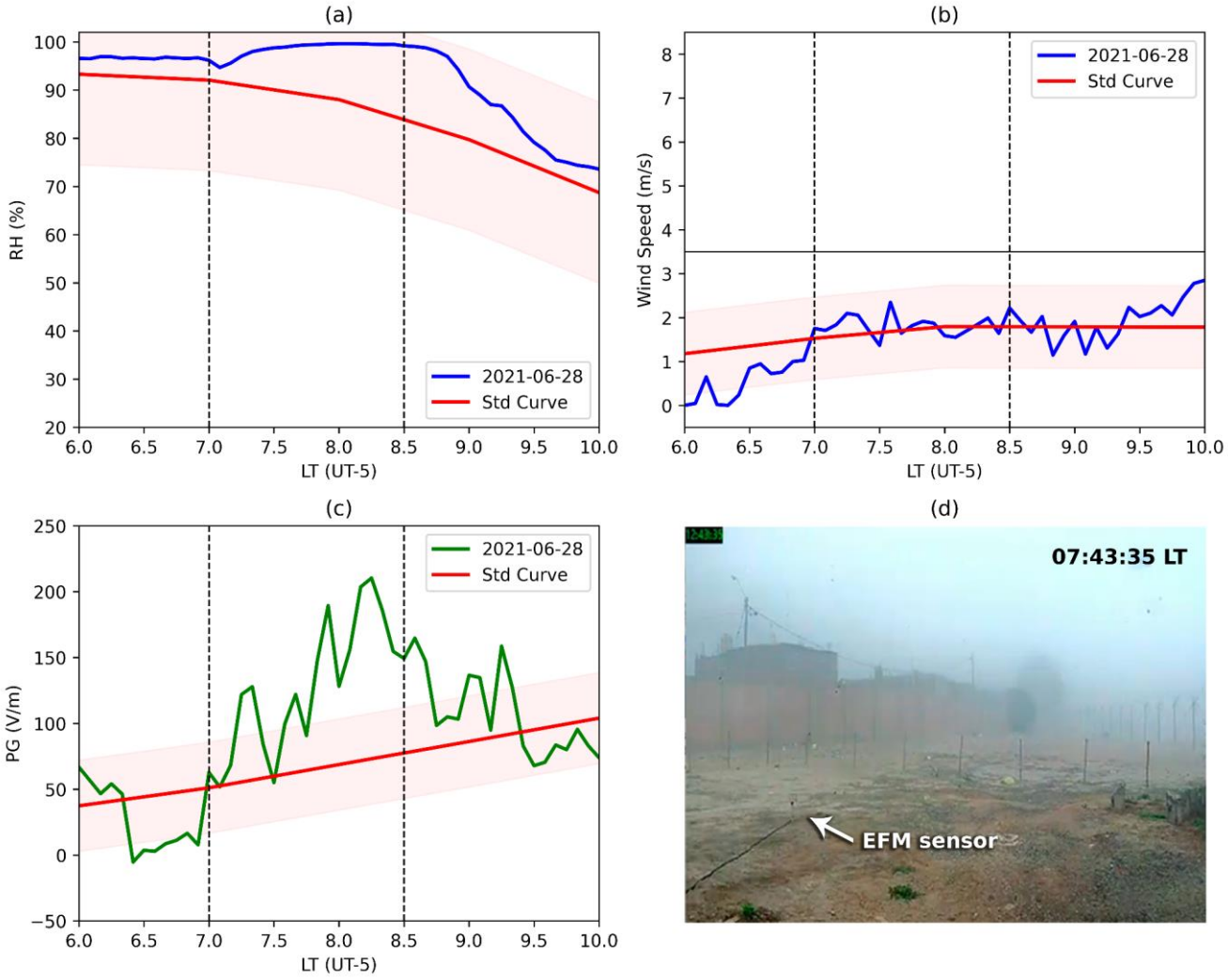

Figure 13. (a) Relative humidity, (b) wind speed, and (c) PG variation during a dense fog event that occurred on June 28, 2021. The red lines represent the monthly variation, for each parameter, under fair weather conditions. The shaded area indicates one standard deviation. (d) Photo taken at 7:43 LT.

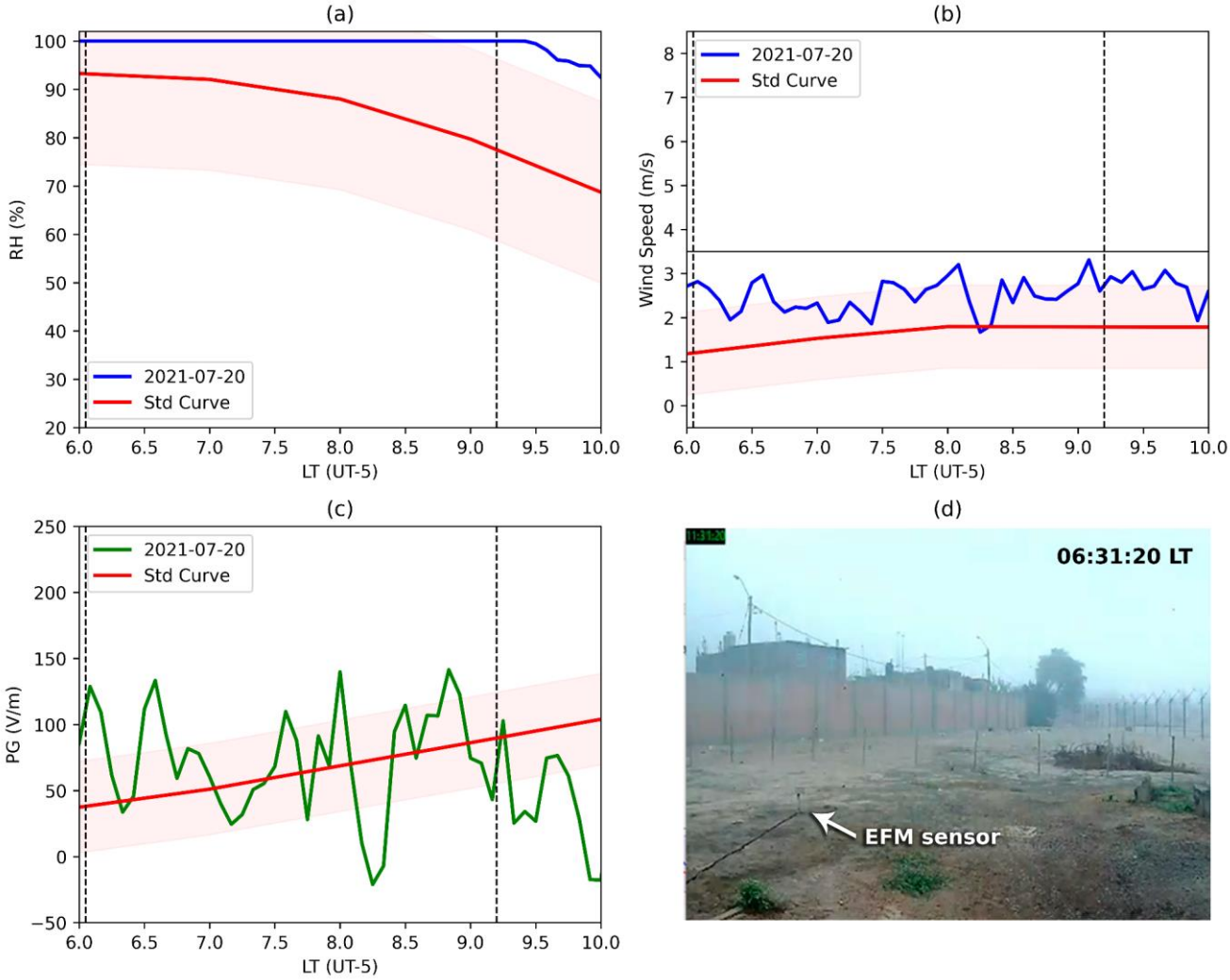

Figure 14. (a) Relative humidity, (b) wind speed, and (c) PG variation during a dense fog event that occurred on July 20, 2021. The red lines represent the monthly variation, for each parameter, under fair weather conditions. The shaded area indicates one standard deviation. (d) Photo taken at 6:31 LT.

3.2. Monthly, Seasonal and Annual standard curves

After correctly identifying the impact of meteorological phenomena on PG, we established the following criteria for constructing monthly, seasonal, and annual standard curves. At Ica station, the following 'fair weather' conditions were applied: PG values with RH < 90%, wind speed < 3.5 m/s, and days without rain precipitation. We will refer to this filtering process as the meteorological criterion. Figure 15 presents the PG monthly standard curves obtained after applying the meteorological criterion. The error bars represent one standard deviation. The figure shows a gradual variation between seasons, with the highest PG values occurring in July (Winter in the South Hemisphere) and the lowest PG values in February (Summer in the South Hemisphere). This trend is well-noted in Figure 16.

Figure 16a presents the PG seasonal standard curves, with shaded areas indicating one standard deviation. A notable distinction in PG amplitude between summer (December, January, February) and winter (June, July, and August) is observed. These findings are similar to previous works reported by Gurmani et al. (2018) in Pakistan, and Lei Li et al. (2023) in China, the UK, and Greece. The authors reported that aerosol and particulate matter (2.5 microns) variations between seasons could account for the PG seasonal variation. In the specific case of Peru, Estevan et al. (2019) reported the occurrence of biomass-burning between July and October, providing support for the observed PG seasonal differences.

Figure 16b presents the PG annual standard curve, obtained using the meteorological criteria (black curve). Additionally, the figure includes the annual mean calculated using a PG range of 0-170 V/m (taking into account the histogram of the PG values shown in Figure 2b). We referred to this as the observational criterion (in red color), which aligns with the method employed by Tacza et al. (2020). Error bars represent one standard deviation in both cases. A high level of agreement is observed when comparing the meteorological and observational criteria (R^2=0.97). This result suggests that in areas lacking meteorological stations installed, the observational criterion can prove to be useful to obtain PG measurements simulating fair weather conditions.

In order to look for global effects on the PG diurnal curve at ICA we used the 'universal' Carnegie curve for comparison. Figure 17a shows the PG seasonal standard curve at ICA compared with the Carnegie curve. Note that the X-axis time is in Universal Time (UT). The dotted vertical lines indicate the time at 3, 8, 14 and 19 UT which are features of the global thunderstorm variation (i.e., minimum at 3 UT, peak of the Asia/Australia chimney at 8 UT, peak of Africa/Europe chimney at 14 UT and peak of the Americas chimney at 19 UT). Despite an acceptable good Pearson correlation coefficient between the PG seasonal standard curves and the Carnegie curve (R=0.88 for summer, R=0.91 for Spring, R=0.93 for Fall and R=0.87 for Winter) there is no agreement when comparing the minimum and any of the maximum times characteristics of the thunderstorm global variation. At Ica, the PG variation shows a broad minimum between ~3 and 10 UT and a maximum at 15 UT in Summer, Spring and Fall, and a maximum at 17 UT in Winter. These findings suggest that the PG diurnal variations are likely associated with local effects instead of global effects.

Figure 17b shows the PG annual standard curve at ICA compared with other PG stations worldwide: Buenos_Aires in Argentina (Velazquez et al., 2024), Gulmarg in India (Afreen et al., 2022), Hermon in Israel (Yaniv et al. 2017), Dilijan in Armenia (Mkrtchyan et al., 2020) and Al Ain in United Arab Emirates (Nicoll et al., 2022). Note that the X-axis time is in the respective Local Time (LT) for each site measurement. There is a good Pearson correlation coefficient between PG at Ica compared with the other stations: R=0.86 (Ica - Buenos Aires), R=0.96 (Ica - Hermon), R=0.94 (Ica - Gulmarg), R=0.97 (Ica - Dilijan) and R=0.92 (Ica - Al Ain). Furthermore, we observed a PG increase after ~6-8 LT for all stations reaching a maximum at around 10-12 LT and then starting to decrease. This PG behavior is more likely associated with local convection. After sunrise, the temperature begins to rise, leading to upward convection and turbulence. This process helps disperse radioactive gases at ground level, such as radon and its radioactive decay products, through attachment to aerosols. As a result, the electrical conductivity at ground level decreases, and the PG increases (Anisimov et al., 2018). The difference in the PG % (percent of the mean) range between all stations is likely associated with specific features of the site environment: Buenos Aires = 59%, Hermon = 59%, Gulmarg = 61 %, Al Ain = 89%, Ica = 134%. Note that the two biggest are Ica and Al Ain which are sites located in arid zones.

Figure 18 shows the PG daily mean during fair weather conditions, employing the meteorological criterion. The dashed black curve represents the monthly average. The seasonal pattern remains consistent across each year. The data gap in 2020 is due to the absence of simultaneous data from the EFM sensor and the meteorological station, which was required to satisfy the meteorological criterion. From this figure, we noted that the seasonal variation does follow the global thunderstorm variation which has higher values during June-July-August and lower values during December-January-February. In other words, the PG seasonal variation does follow the seasonal variation of the GEC. However, it is more likely that this PG behavior is associated with the biomass-burning, which is more intense during the months between July and October (Estevan et al., 2019).

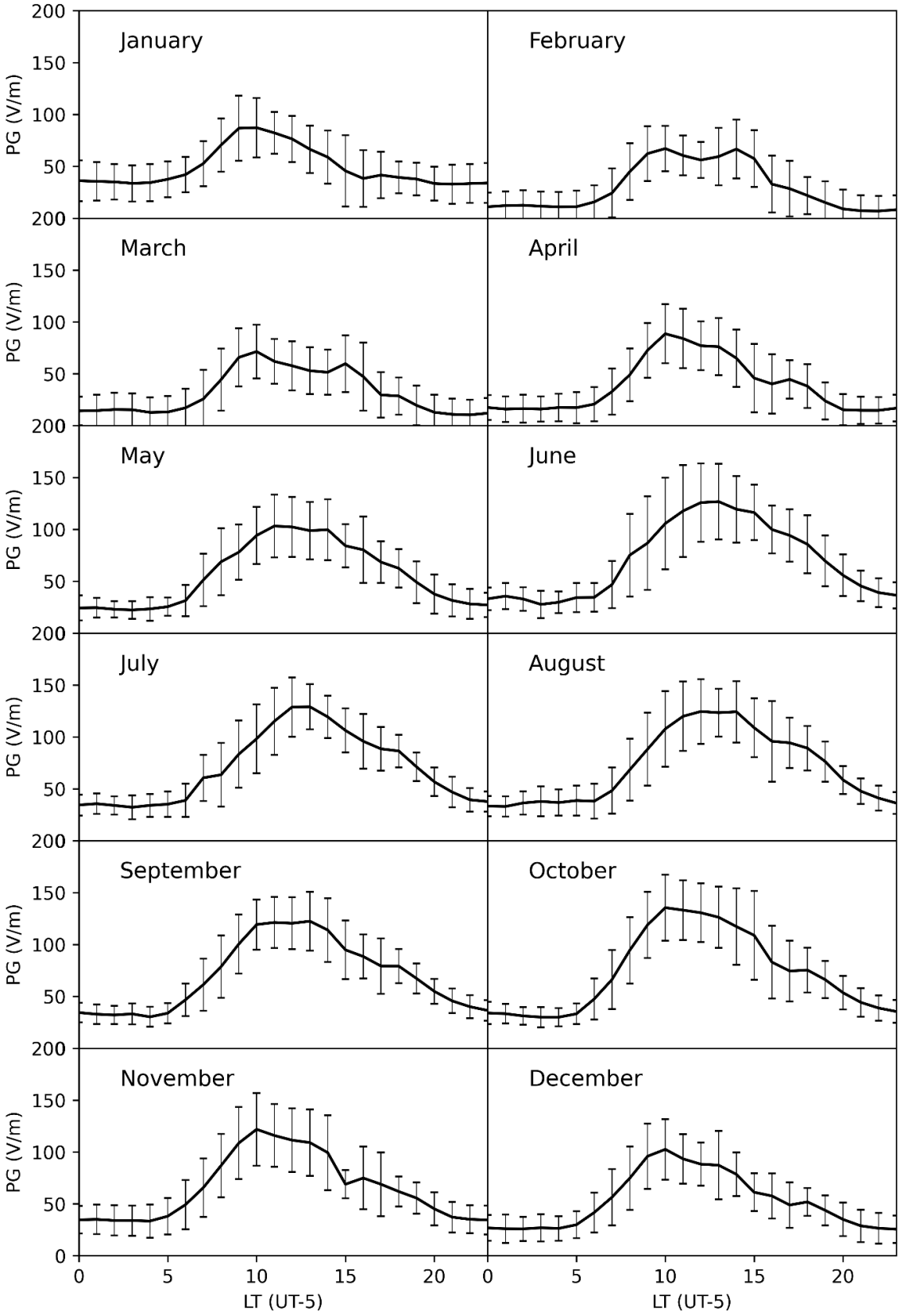

Figure 15. PG monthly standard curves, utilizing meteorological criteria for fair weather, for the period between 2019 and 2022. The error bars indicate one standard deviation.

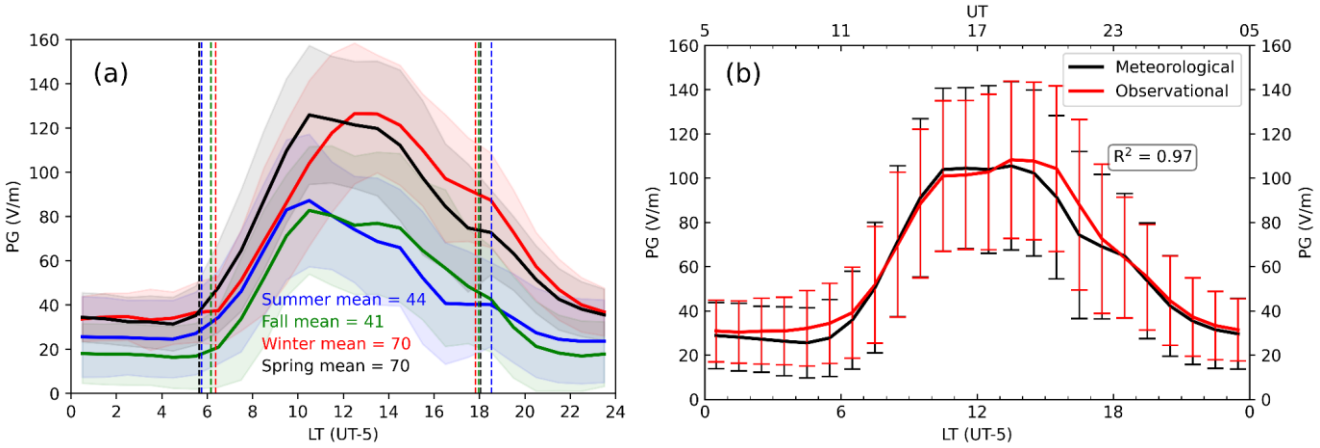

Figure 16. (a) PG seasonal standard curves, based on meteorological criteria for fair weather. The shaded areas represent one standard deviation. The dashed vertical lines indicate the times of sunrise and sunset for each season. (b) PG annual standard curve using the meteorological (black) and observational (red) criteria. The error bars represent one standard deviation of the mean (1σ). The study period is between 2019 and 2022.

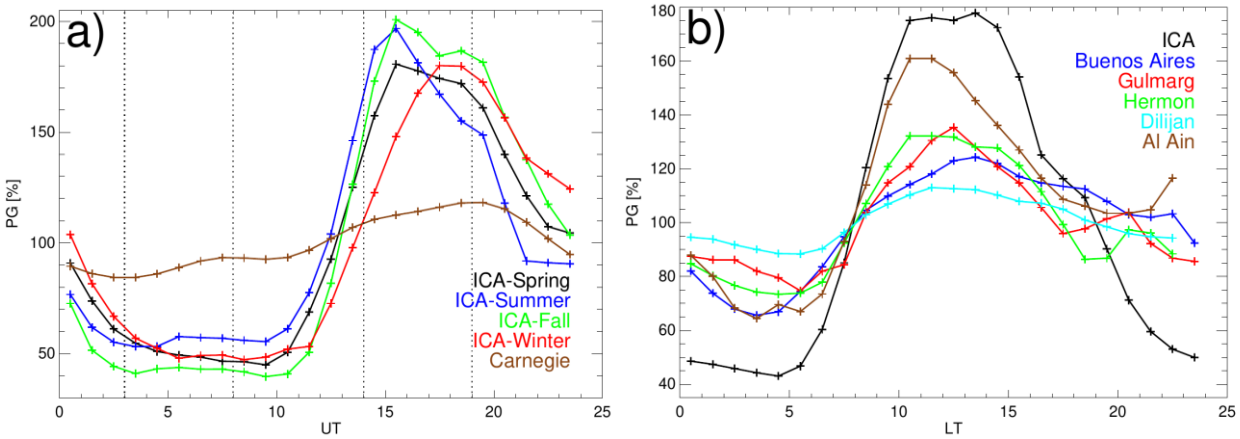

Figure 17. (a) ICA PG seasonal standard curves compared with the Carnegie curve, plotted as percent of the mean, in Universal Time (UT). Vertical dotted lines indicate the times at 3, 8, 14 and 19 UT. (b) ICA PG annual standard curve compared with other PG stations worldwide, plotted as percent of the mean, in Local time (LT). See the text for details.

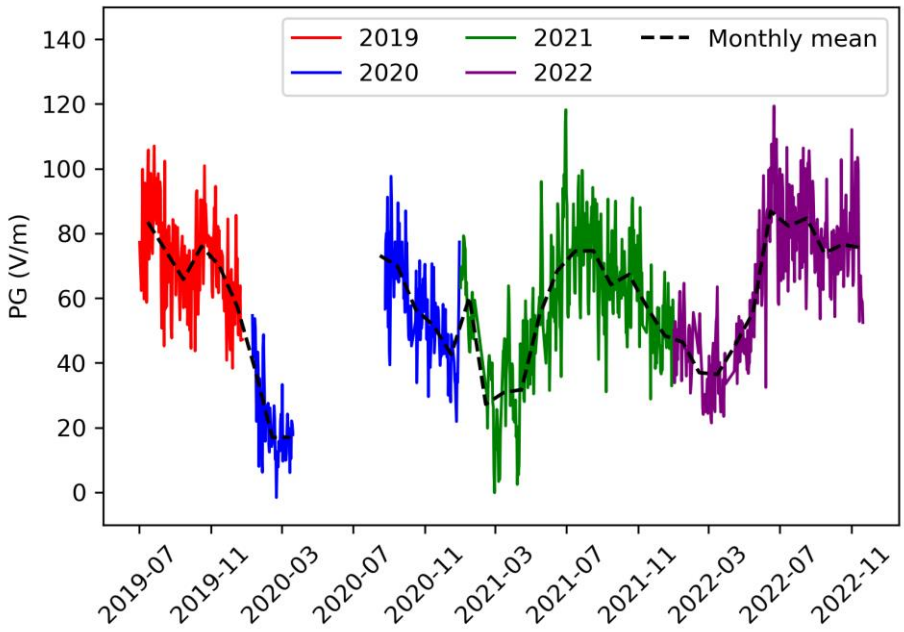

Figure 18. PG daily averages (solid color lines) and PG monthly averages (dashed black line) in fair weather using the meteorological criteria.

3.3 Spectral analysis

Figure 19 displays the wavelet analysis using the hourly amplitudes of PG for the entire dataset duration (from March 2018 until December 2022). The PG values are selected based on the observational criteria to minimize data gaps, i.e., positive PG values in the range between 0-170 v/m. In Figure 19a, the time series is shown, with data gaps corresponding to periods of power supply interruption. In order to apply wavelet analysis, it is necessary to have a constant time step between samples. To fill these gaps, the moving average of the original time series is computed with a time window length of 3,072 hours. This filling procedure minimizes the introduction of artifacts in the wavelet analysis (Macotela et al., 2019).

Figure 19b presents the continuous wavelet power spectra, which have been corrected by their scales (Liu et al., 2007). The contours represent the magnitude of the matches between the phases of the time series and the wavelet. The color bar indicates the amplitude of these contours, ranging from blue to red. The black curves represent the cone of influence. Figure 19c displays the global wavelet power spectra. The dashed line corresponds to the 98% confidence level for a red noise process. Powers above this line are considered significant, and their maxima are indicated by dashed horizontal lines. It can be observed that the 1-day, 45-day, 188-day, and 360-day periodicities exhibit significance in the analysis.

The 1-day, 188-day and 360-day are related to the well-known diurnal, semiannual and annual PG variation. This was observed in the time series plotted in Figures 15, 16, 17 and 18. As explained earlier, these periods are related to local effects at Ica station. Less explored in the literature, is the 45-day period. We observed that this period was more intense during the first months of 2018 (Figure 19b). Tacza et al. (2022) connected this period with the Madden-Julian Oscillation (MJO). The MJO is characterized by large-scale linked patterns of atmospheric circulation and deep convection. It is the primary driver of intraseasonal variations in the tropical atmosphere. Therefore, it is not surprising that the MJO can modulate the GEC. This has been recently demonstrated by Kozlov et al. (2023). Tacza et al. (2022) found a connection between the PG and MJO through a cross-wavelet analysis. Furthermore, the authors found a similar 45-day intense period during the first months of 2018 for Casleo (Argentina) and Sodankyla (Finland) PG stations. The time interval between January and March 2018 has been cataloged as one of the strongest MJO events (Barret, 2018). These results suggest that at Ica we can also observe the global effect of the GEC.

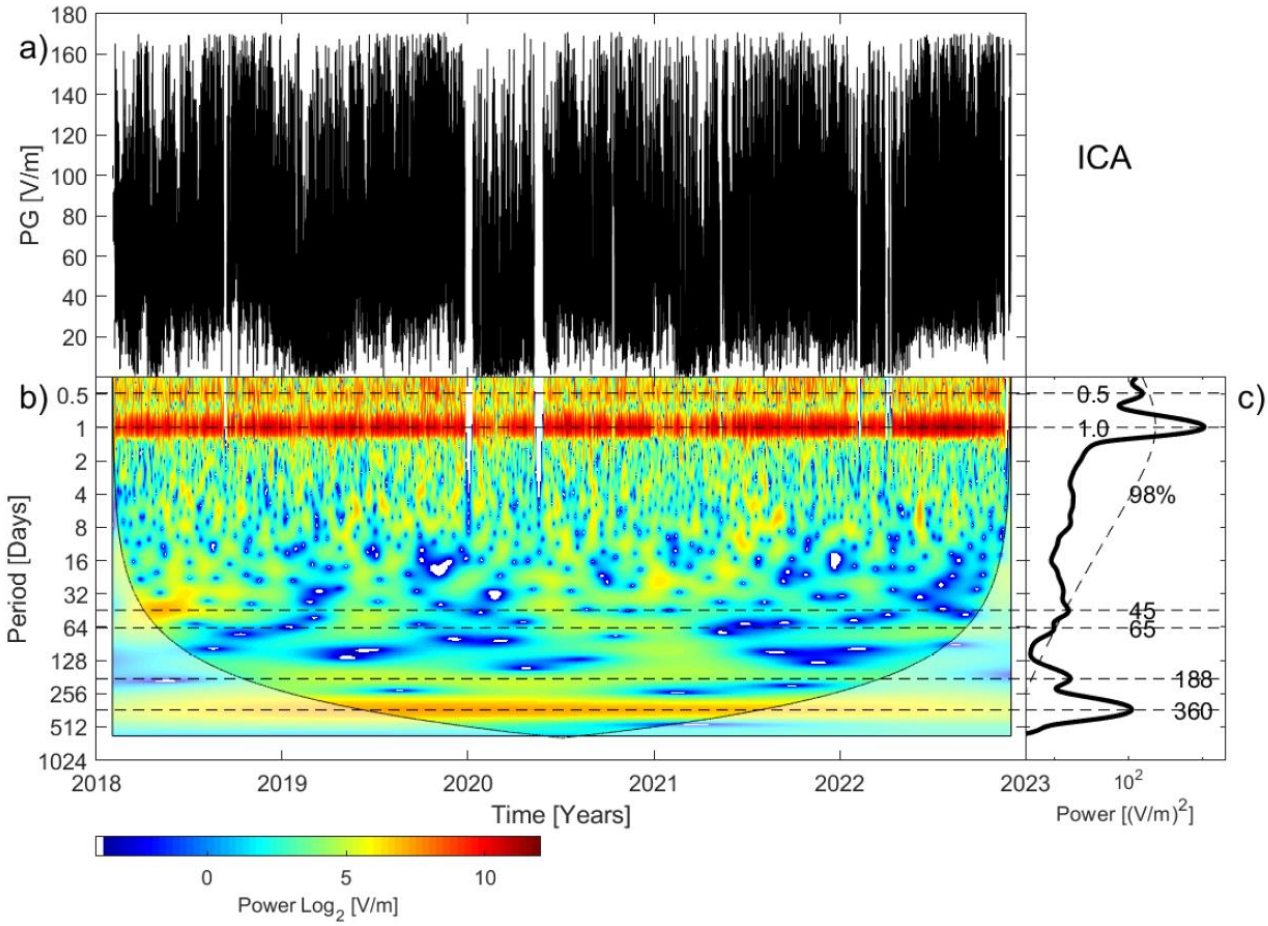

Figure 19. Wavelet analysis for Ica station. (a) Hourly average of the PG amplitude ranging from 0 to 170 V/m. Gaps in the data indicate missing information. (b) Contours representing the real part of the wavelet power spectra of PG in the time-period domain. The colors of the contours indicate the minimum and maximum magnitude, ranging from blue to red. These contours highlight the matches between the phases of the time series and the wavelet. The white shadowed lateral edges represent values within the cone of influence. (c) The global wavelet power spectrum, which provides an overview of the power distribution across different time scales. Horizontal lines indicate the most significant oscillations, while the dashed curve represents the 98% confidence level.

4. Summary and conclusions

In summary, this study has investigated the factors influencing the potential gradient (PG) in Ica, a city located in the coastal desert region of southern Peru. The analysis revealed that local meteorological conditions play a significant role in determining the variations in PG.

Rainfall events in Ica, which are generally low-intensity and sporadic, were found to cause significant variations in PG, leading to the exclusion of rainy days from the standard curve. Strong winds that characterize the Ica region, influenced by local topography and the sea breeze, showed a clear impact on the PG diurnal variation. Different wind directions led to increases or decreases in PG due to aerosol transport from various sources, occasionally resulting in dust storms known as "Vientos Paracas" (Quijano, 2013). A threshold of 3.5 m/s was found to prevent the effects of the sea breeze and dust lifting, which caused a significant increase in PG over several hours, similar to the study conducted by Nicoll et al. (2022) in arid zones. However, during sea breeze events in Ica, visibility reduction was not observed; further investigation utilizing more in-depth studies and additional equipment is warranted. Additionally, the proximity of the South Pacific Anticyclone to the coast, particularly during spring, further modulates these wind patterns, as evidenced by increased PG dispersion in this season.

Similar PG effects as observed in other parts of the world were found for the Paracas dust storms (Rudge, 1913; Demon et al., 1953; Renno et al., 2004). Additionally, the origin of these winds aligns with the dust sources identified in Ica through the study conducted by Briceño-Zuluaga et al. (2017), both using the HYSPLIT model and local wind direction data. It is important to note that there are some cases where we observed PG decreases without a reduction in visibility, some of which preceded the Paracas storms. This can be attributed to the space charge generated by the low density of dust suspended in the air, which has been widely documented in the literature (Rudge, 1913; Kamra, 1972; Zhang et al., 2017). The ability to detect changes in the electric field prior to dust events, as discussed in our study, offers valuable insights for the prediction and forecasting of dust storms.

The impact of dust devils on PG was particularly notable. We recorded three key events demonstrating transient PG surges, indicative of positively charged areas within dust devils, supporting findings by Lorenz et al. (2016). Conversely, direct overhead passages of dust devils caused PG decreases, likely due to the shielding effect of negatively charged dust, as discussed by Freier (1960) and Farrell et al. (2004). The most significant event exhibited a complex PG pattern, underscoring the nuanced interaction between dust devils and the electric field.

Fog events also demonstrated an influence on PG, with dense fog leading to increased PG on 5% of foggy days, while less dense fog resulted in rapid oscillations in PG on 95% of foggy days and nearly 40% of winter days. The increase in PG can be attributed to the decrease in the electrical conductivity of the air, a notion well-established in the scientific literature (Anisimov et al., 2005; Bennet and Harrison, 2009; Yair and Yaniv, 2023). On the other hand, the rapid fluctuations in PG are likely associated with changes in the altitude of cloud bases. Given the typically negative charge at the base of cloud layers, alterations in their height significantly impact the PG (Harrison et al., 2019). Notably, this concept also applies to fog, which is essentially a form of stratus cloud located just above the ground (Lakra and Avishek, 2022). However, it is important to mention that this conclusion requires further validation, as precise measurements provided by a ceilometer are currently lacking.

The analysis of monthly, seasonal, and annual standard curves reveals a significant impact of aerosols and PM 2.5 concentrations on the variation in PG. Moreover, the PG stations in Lima and Huancayo, Peru, exhibit a similar seasonal variation to that observed in Ica (Tacza et al., 2020). The PG seasonal variation is likely driven by differences in seasonal aerosol concentrations, primarily influenced by biomass-burning activities, as extensively documented in Peru from July to October (Estevan et al., 2019). However, it is important to note that this model remains speculative due to the lack of in situ measurements of aerosols in Ica. Taking this into consideration, these activities would contribute significantly to the observed seasonal differences, resulting in a distinct PG amplitude between summer and winter. This understanding lays a crucial groundwork for future research on the relationship between atmospheric aerosols, including those originating from biomass-burning, and variations in PG.

It's important to note that the local effects caused by convective processes in the PG diurnal variation occur consistently on a daily basis, and as a result, they are reflected in the standard curves for monthly, seasonal, and annual measurements. By comparing the PG values measured on the day of a particular phenomenon with the corresponding values in the monthly, seasonal, or annual standard curve, we can observe daily disturbances in the PG values associated with external geophysical phenomena.

The wavelet analysis performed in this study using hourly amplitudes of PG provided valuable information on the presence of short-term oscillations and their significant frequencies, which can be useful for understanding the dynamics of the PG in Ica. At Ica, significant periodicities of 1 day, 188 days, and 360 days were observed, which correspond to the well-known diurnal, semiannual and annual periodicities. The 45-day periodicity is likely associated with the Madden-Julian Oscillation, which was more intense during the months between January and March 2018. This was also found for other PG stations worldwide suggesting that we can also observe global effects at Ica.

While this study provides valuable insights into various aspects of the PG and its relationship with meteorological factors, it highlights the necessity for further research on specific topics. These topics include investigating the effects of sea breezes and dust storms using additional equipment (e.g. ceilometer), validating the relationship between fog and PG with specific equipment and techniques, and conducting in situ measurements of aerosols. By addressing these gaps, we can enhance our understanding of the interactions between meteorological conditions and the PG in arid regions. This comprehensive examination of the factors influencing PG in Ica contributes significantly to advancing our knowledge in this field.

Acknowledgements

The authors would like to thank the two anonymous reviewers for valuable comments that improved the quality of the paper.

JPR thanks funding agencies CNPq (project:311927/2022-0) and CAPES (project:88881.310386/2018-01). RR expresses gratitude to CNPq (Proc. 141576/2023-5 - GD).

Data availability

Ica PG data is available from the GloCAEM database:
http://data.ceda.ac.uk/badc/glocaem/data/.

References

Afreen, S., Victor, N.J., Nazir, S. et al. Fair-weather atmospheric electric field measurements at Gulmarg, India. J Earth Syst Sci 131, 7 (2022). https://doi.org/10.1007/s12040-021-01745-5

Anisimov, S.V., Galichenko, S.V., Aphinogenov, K.V., Prokhorchuk, A.A., 2018. Evaluation of the atmospheric boundary-layer electrical variability. Bound.-Layer Meteorol. 167 (2), 327–348.

American Meteorological Society, 2023: Fog. Glossary of Meteorology, http://glossary.ametsoc.org/wiki/fog.

Anisimov, S., Mareev, E.A., Shikhova, N.M., Sorokin, A.E., Dmitriev, E.M., 2005. On the electro–dynamical characteristics of the fog. Atmospheric Research. 76. 16-28. 10.1016/j.atmosres.2004.11.026.

Bagnold, R.A., 2012. The Physics of Blown And Desert Dunes. Courier Corporation

Barrett, B. S. (2019). Connections between the Madden-Julian Oscillation and surface temperatures in winter 2018 over eastern North America. Atmospheric Science Letters, 20(1), e869.

Bennett A.J., Harrison R.G., 2007. Atmospheric electricity in different weather conditions. Weather – October 2007, Vol. 62, No. 10

Bennett A.J., Harrison R.G., 2009. Evidence for global circuit current flow through water droplet layers, Journal of Atmospheric and Solar-Terrestrial Physics, Volume 71, Issue 12, 2009, Pages 1219-1221, ISSN 1364-6826,

Bo, T.-L., Zheng, X.-J., 2013. A field observational study of electrification within a dust storm in Minqin, China, Aeolian Res., 8, 39–47.

Briceño-Zuluaga F., Castagna, A., Rutllant, J., Aqueveque, V., Caquineau, S., Sifeddine, A., Velazco, F., Gutiérrez, D., Cardich, J., 2017. Paracas dust storms: Sources, trajectories and associated meteorological conditions. Atmospheric Environment. 165. 10.1016/j.atmosenv.2017.06.019.

Correa, D., Chamorro, A., Tam, J., 2020. Clasificación pentadal de vientos frente a la costa peruana. Revista de Investigación de Física, 23(3), 61–65.

Crozier, W.D., 1964. The Electric field of New Mexico dust devil. J. Geophys. Res. 69, 5427–5429.

Crozier, W.D., 1970. Dust devil properties. J. Geophys. Res. 75, 4583–4585

Davila, C., Cubas Saucedo, F., Laura, W., Ita Vargas, T., Porras, P., Castro, A., Trebejo, I., Urbiola, J., Avalos, G., Villena, D., Valdez, M., Rodríguez Zimmermann, D., Menis, L., 2021. Atlas de temperaturas del aire y precipitación del Perú. SENAMHI.

Demon, L., Defelice. P., Gondet, H., Kast, Y. and Pontier, L., 1953. Premiers résultats obtenus au cours du printemps 1953, J. Rech. C. N. R. S., 24, 126.

Dewitte, B., Illig, S., Renault, L., Goubanova, K., Takahashi, K., 2011. Modes of covariability between sea surface temperature and wind stress intraseasonal anomalies along the coast of Peru from satellite observations (2000-2008). JGR, vol 116. doi:10.1029/2010JC006495

Duff, N., and Lacks, D.J., 2008. Particle dynamics simulations of triboelectric charging in granular insulator systems, J. Electrost., 66, 51.

Esposito, F., Molinaro, R., Popa, C.I., Molfese, C., Cozzolino, F., Marty, L., Taj-Eddine, K., Di Achille, G., Franzese, G., Silvestro, S., Ori, G.G., 2016. The role of the atmospheric electric field in the dust-lifting process. Geophys. Res. Lett. 43, 5501–5508.

Estevan, R., Martínez-Castro, D., Suarez-Salas, L., Moya, A., Silva, Y., 2019. First two and a half years of aerosol measurements with an AERONET sunphotometer at the Huancayo Observatory, Peru, Atmospheric Environment: X, Volume 3, 2019, 100037, ISSN 2590-1621.

Farrell, W.M., Smith, P.H., Delory, G.T., 2004. Electric and magnetic signatures of dust devils from the 2000–2001 MATADOR desert tests. J. Geophys. Res. 109, E03004.

Franzese, G., Esposito, F., Lorenz, R., Silvestro, S., Popa, C.I., Molinaro, R., Cozzolino, F., Molfese, C., Marty, L., Deniskina, N., 2018. Electric properties of dust devils. Earth Planet. Sci. Lett. 493, 71–81.

Freier, G.D., 1960. The electric field of a large dust devil. J. Geophys. Res. 65, 3504.

Gay, S.P., 2005. Blowing sand and surface winds in the Pisco to Chala Area, Southern Peru. Journal of Arid Environments 61. 101–117.

Grinsted, A., Moore, J.C., Jevrejeva, S., 2004. Application of the cross wavelet transform and wavelet coherence to geophysical time series. Nonlinear Process. Geophys. 11, 561–566.

Gurmani, S.F., Ahmad, N., Tacza, J., Iqbal, T., 2018. First seasonal and annual variations of atmospheric electric field at a subtropical station in Islamabad, Pakistan. Journal of Atmospheric and Solar-Terretrial Physics, 179, 441–449.

785
786 Haldoupis, C., Rycroft, M., Williams, E., Price, C., 2017. Is the “Earth-ionosphere capa-citor” a valid
787 component in the atmospheric electric circuit? Journal of Atmospheric and Solar-Terretrial Physics,
788 164, 127–131.
789
790 Haney, E.M., Grolier, M.J., 1991. Geologic map of major quaternary eolian features, northern and
791 central coastal Peru. U.S. Geological Survey Miscellaneous Investigation I-2162.
792
793 Harrison R.G., 2011. Fair weather atmospheric electricity. J. Phys.: Conf. Ser. 301 012001
794
795 Harrison, R.G., 2013. The Carnegie Curve. Surveys in Geophysics, 34, 209–232.
796
797 Harrison, R. G., Nicoll K. A. and Aplin K. L., 2017. Evaluating stratiform cloud base charge remotely,
798 Geophys. Res. Lett., 44, 6407–6412, doi:10.1002/2017GL073128.
799
800 Harrison, R.G., Marlton G.J., Aplin K.L., Nicoll K.A., 2019. Shear-induced electrical changes in the
801 base of thin layer-cloud. Q J R Meteorol Soc. 2019;145:3667–3679
802
803 Imyanitov, I.M., 1957. Pribory i metody dlya izucheniya elektrichestva atmosfery (Devices and
804 Methods for Study of Electricity of Atmosphere), Moscow: Gostekhizdat, 1957, pp. 189–193
805
806 Kamra, A. K., 1972. Measurements of the electrical properties of dust storms, J. Geophys. Res., 30,
807 5856–5869.
808
809 Karagioras A. and Kourtidis K., 2021. A Study of the Effects of Rain, Snow and Hail on the
810 Atmospheric Electric Field near Ground. Atmosphere 2021, 12, 996.
811
812 Kozlov, A.V.; Slyunyaev, N.N.; Ilin, N.V.; Sarafanov, F.G.; Frank-Kamenetsky, A.V. The Effect of
813 the Madden–Julian Oscillation on the Global Electric Circuit. Atmos. Res. 2023, 284, 106585.
814
815 Lakra, K., Avishek, K., 2022. A review on factors influencing fog formation, classification,
816 forecasting, detection and impacts. Rendiconti Lincei. Scienze Fisiche e Naturali (2022) 33:319–353.
817
818 Li, L., Chen, T., Song, J., Ti, S., Wang, S., Cai, C., Li, W., Luo, J., 2023. Comparison of the
819 Atmospheric Electric Field from Three Global Stations in 2021. Universe 2023, 9, 112
820
821 Liu, C., Williams, E., Zipser, E.J., Burns, G., 2010. Diurnal variations of global thunderstorms and
822 electrified shower clouds and their contribution to the global electric circuit. J. Atmos. Sci. 67 (2),
823 309–323.
824
825 Liu, Y., San Liang, X., Weisberg, R.H., 2007. Rectification of the Bias in the Wavelet Power
826 Spectrum. J. Atmos. Ocean. Technol. 24 (12), 2093–2102.
827
828 Lorenz, R.D., Neakrase, L.D.V., Anderson, J.P., Harrison, R.G., Nicoll, K.A., 2016. Point discharge
829 current measurements beneath dust devils. Journal of Atmospheric and Solar-Terretrial Physics, 150
830 55–60.
831
832 MacGorman, D.R., Rust, W.D., 1998. The Electrical Nature of Storms. Oxford University Press 0-19-
833 507337-1 (423 pp.)
834
835 Macotela, E. L., Clilverd, M., Manninen, J., Moffat-Griffin, T., Newnham, D. A., Raita, T., Rodger,
836 C.J., 2019. D-region high-latitude forcing factors. J. Geophys. Res. Space Phys. 124 (1), 765–781.

Mkrtchyan, H., Karapetyan, G., & Aslanyan, D. (2020). Atmospheric electric field variations during fair weather and thunderstorms at different altitudes. Journal of Atmospheric and Solar-Terrestrial Physics, 211, 105452. https://doi.org/10.1016/j.jastp.2020.105452

Nicoll, K.A., Harrison, R.G., Barta, V., Bor, J., Brugge, R., Chillingarian, A., Chum, J., Georgoulias, A.K., Guha, A., Kourtidis, K., Kubicki, M., Mareev, E., Matthews, J., Mkrtchyan, H., Odzimek, A., Raulin, J.-P., Robert, D., Silva, H.G., Tacza, J., Yair, Y., Yaniv, R., 2019. A global atmospheric electricity monitoring network for climate and geophysical research, Journal of Atmospheric and Solar-Terrestrial Physics, 184, 18–29.

Nicoll, K.A., Readle, A., Al Kamali, A., Harrison, R.G., 2022. Surface atmospheric electric field variability at a desert site, Journal of Atmospheric and Solar-Terrestrial Physics, 241, 2022, 105977, ISSN 1364-6826.

Quijano, J., 2013. Estudio numérico y observacional de la dinámica de viento paracas, asociado al transporte eólico hacia el océano frente a la costa de Ica - Perú. (Master's thesis, UPCH).

Rennó, N.O., Abreu, V.J., Koch, J., Smith, P.H., Hartogensis, O.K., De Bruin, H.A., Burose, D., Delory, G.T., Farrell, W.M., Watts, C.J. and Garatuza, J., 2004. MATADOR 2002: a pilot field experiment on convective plumes and dust devils. J. Geophys. Res., 109(E7). E07001, doi:https://doi.org/10.1029/2003JE002219, 2004.

Rudge, W.A.D., 1913. Atmospheric electrification during South African dust storms, Nature, 91, 31–32.

Rycroft, M.J., Israelsson, S., Price, C., 2000. The global atmospheric electric circuit, solar activity and climate change. Journal of Atmospheric and Solar-Terretrial Physics, 62: 1563–1576.

Rycroft, M.J., Harrison, R.G., Nicoll, K.A., Mareev, E.A., 2008. An Overview of Earth's Global Electric Circuit and Atmospheric Conductivity. Space Sci Rev 137, 83–105.

Secker, P.E., 1975. The design of simple instrumentation for measurement of charge on insulating surfaces. J. Electrost. 1 (1), 27–36.

Tacza, J., Raulin, J.-P., Macotela, E., Marun, A., Fernandez, G., Bertoni, F., Lima, L., Samanes, J., Buleje, Y., Correia, E., Alves, G., Makita, K., 2020. Local and global effects on the diurnal variation of the atmospheric electric field in South America by comparison with the Carnegie curve. Atmospheric Research, 240, 104938.

Tacza J., Nicoll, K.A., Macotela, E.L., Kubicki, M., Odzimek, A., Manninen, J., 2021. Measuring Global Signals in the Potential Gradient at High Latitude Sites. Front. Earth Sci. 8:614639.

Tacza J., Nicoll, K.A., Macotela E., 2022. Periodicities in fair weather potential gradient data from multiple stations at different latitudes, Atmospheric Research, Volume 276, 2022, 106250, ISSN 0169-8095.

Torrence, C., Compo, G., 1998. A practical guide to wavelet analysis. Bulletin of American Meteorological Society 79, 61–78.

Torreson OW, Parkinson WC, Gish OH, Wait GR (1946) Ocean atmospheric-electric results (Scientific Results of Cruise VII of the Carnegie during 1928–1929 under command of Captain J. P.

Ault, vol 3). Researches of the Department of Terrestrial Magnetism. Carnegie Institution of Washington Publication, vol 568

Telang, A.V.R., 1930. The influence of rain on the atmospheric-electric field. Terrestrial Magnetism and Atmospheric Electricity. Vol. 35, Issue 3, 125-131.

Velazquez, Y., Nicora, G., Galligani, V., Wolfram, E., Salio, P., D'Elia, R., 2024. Exploring the global thunderstorm influence on the fair weather electric field in Buenos Aires. Atmospheric Research, 299, 107182, 2024.

Williams, E., Nathou, N., Hicks, E., Pontikis, C., Russell, B., Miller, M., Bartholomew, M.J., 2008. The electrification of dust-lofting gust fronts ('haboobs') in the Sahel, Atmospheric Research, Volume 91, Issues 2–4, 2009, Pages 292-298, ISSN 0169-8095,

Yair, Y., Yaniv, R., 2023. The Effects of Fog on the Atmospheric Electrical Field Close to the Surface. Atmosphere 2023, 14, 549.

Yaniv R, Yair Y, Price C, Mkrtchyan H, Lynn B, Reymers A (2017) Ground-based measurements of the vertical E-field in mountainous regions and the "Austausch" effect. Atmos Res 189:127–133.

Zhang, H., Bo, T-L., Zheng, X., 2017. Evaluation of the electrical properties of dust storms by multi-parameter observations and theoretical calculations, Earth and Planetary Science Letters, Volume 461, 2017, Pages 141-150, ISSN 0012-821X.